Charged-particle production as a function of multiplicity and transverse spherocity in pp collisions at √s=5.02 and 13 TeV

(ALICE Collaboration) Acharya, S.; ...; Antičić, Tome; ...; Erhardt, Filip; ...; Gotovac, Sven; ...; Jerčić, Marko; ...; ...

THE EUROPEAN
PHYSICAL JOURNAL C

Charged-particle production as a function of multiplicity and transverse spherocity in pp collisions at $\sqrt{s} = 5.02$ and $13\,\mathrm{TeV}$

ALICE Collaboration[*]

CERN, 1211 Geneva 23, Switzerland

Abstract We present a study of the inclusive charged-particle transverse momentum (p_T) spectra as a function of charged-particle multiplicity density at mid-pseudorapidity, $dN_{ch}/d\eta$, in pp collisions at $\sqrt{s} = 5.02$ and $13\,\mathrm{TeV}$ covering the kinematic range $|\eta| < 0.8$ and $0.15 < p_T < 20\,\mathrm{GeV}/c$. The results are presented for events with at least one charged particle in $|\eta| < 1$ (INEL > 0). The p_T spectra are reported for two multiplicity estimators covering different pseudorapidity regions. The p_T spectra normalized to that for INEL > 0 show little energy dependence. Moreover, the high-p_T yields of charged particles increase faster than the charged-particle multiplicity density. The average p_T as a function of multiplicity and transverse spherocity is reported for pp collisions at $\sqrt{s} = 13\,\mathrm{TeV}$. For low- (high-) spherocity events, corresponding to jet-like (isotropic) events, the average p_T is higher (smaller) than that measured in INEL > 0 pp collisions. Within uncertainties, the functional form of $\langle p_T \rangle (N_{ch})$ is not affected by the spherocity selection. While EPOS LHC gives a good description of many features of data, PYTHIA overestimates the average p_T in jet-like events.

1 Introduction

Proton-proton collisions at the Large Hadron Collider (LHC) energies have unveiled features very similar to the ones observed in heavy-ion collisions [1]. The previous consensus of the heavy-ion community was that the partonic system created in nuclear collisions needs a large volume to thermalize and to lead to phenomena like collective flow. However, radial [2–4] and anisotropic flow [5], as well as strangeness enhancement [6], are also observed in pp and p-A collisions when they are studied as a function of event multiplicity. Surprisingly, with the same level of precision, microscopic and macroscopic approaches describe qualitatively well the observed features in pp collisions. While macroscopic models incorporate hydrodynamical evolution of the system [7], the others include overlapping strings [8], string percolation

[9], multi-parton interactions and color reconnection [10,11]. The multiphase transport model [12], as well as the fragmentation of saturated gluon states [13,14], is able to describe some features of data.

The inclusive transverse momentum (p_T) spectrum of charged particles carries information of the dynamics of soft and hard interactions. On one hand, the high-p_T ($p_T > 10\,\mathrm{GeV}/c$) particle production is quantitatively well described by perturbative QCD (pQCD) calculations; on the other hand, the understanding of particle production at low-p_T has to resort to phenomenological QCD inspired models. Most of the new effects discovered in pp collisions have been unveiled in the low- ($p_T < 2\,\mathrm{GeV}/c$) and intermediate- ($2 \leq p_T < 10\,\mathrm{GeV}/c$) p_T domains [2–6]. The present paper reports a novel multi-differential analysis aimed at understanding charged-particle production associated to partonic scatterings with large momentum transfer and their possible correlations with soft particle production.

The transverse momentum distributions are reported for two multiplicity estimators which cover different pseudorapidity regions. The estimators are based on either the total charge deposited in the forward detector (covering the pseudorapidity regions $2.8 < \eta < 5.1$ and $-3.7 < \eta < -1.7$) or on the number of tracks in the pseudorapidity region $|\eta| < 0.8$. The forward multiplicity estimator is commonly used by the ALICE collaboration to minimize the possible autocorrelations induced by the use of the mid-pseudorapidity estimator. One such examples is the "fragmentation bias" [15], which is the correlation between jet fragments and event multiplicity arising when the particle's p_T and event multiplicity are both measured within the same pseudorapidity interval [16]. For each estimator, we defined different multiplicity classes based on either the number of tracks at mid-pseudorapidity ($|\eta| < 0.8$) or the signal in the forward detectors. It is worth mentioning that a similar study has been performed by ALICE using p-Pb data; the results showed different modifications of the spectral shapes depending on the multiplicity estimators which were used [17]. To disentangle the energy and multiplicity dependence, for a given

[*] e-mail: alice-publications@cern.ch

multiplicity class, the p_T distributions are measured for pp collisions at $\sqrt{s} = 5.02$ and 13 TeV. Particle production from intermediate to high p_T ($> 4\,\mathrm{GeV}/c$) is studied by fitting a power-law function to the invariant yield, and studying the multiplicity and energy dependence of the exponent. This has been proposed in Ref. [18] as a way to characterize the high-p_T tails of different systems and energies in a convenient way that may make the comparison for the different systems more straightforward.

Finally, we explore a new approach, which has been proposed to study multi-parton interaction effects in pp collisions. Transverse spherocity [19], hereinafter referred to as spherocity, has been proven to be a valuable tool to discriminate between jet-like and isotropic events [20] associated with an underlying event activity which is either suppressed or enhanced. The previous measurement of average transverse momentum of inclusive charged particles as a function of event multiplicity [21] is now explored adding a new dimension: the event shape characterized by spherocity. The aim of this study is to investigate the importance of jets in high-multiplicity pp collisions and their contribution to charged-particle production at low p_T.

The paper is organized as follows: Sect. 2 describes the run conditions during the data taking and the main detectors used in the present analysis. Section 3 outlines the analysis details for the event and track selection, as well as the definitions of the different event classes. The correction procedures and the estimation of the systematic uncertainties are summarized in Sects. 4 and 5, respectively. Results and discussions are presented in Sect. 6. Finally, our summary and conclusions are reported in Sect. 7.

2 The ALICE apparatus

The main detectors used in the present work are the Inner Tracking System (ITS), the Time Projection Chamber (TPC) and the V0 detector. The ITS and TPC detectors are both used for primary vertex and track reconstruction. The V0 detector is used for triggering and for background rejection. More details concerning the full ALICE detector system can be found in Ref. [22].

The central barrel covers the pseudorapidity region $|\eta| < 0.8$ for full-length tracks. The main central-barrel tracking devices are the ITS and the TPC, which are located inside a solenoid magnet providing a 0.5 T magnetic field allowing the tracking of particles from 0.15 GeV/c. The ITS is composed of six cylindrical layers of high-resolution silicon tracking detectors. The innermost layers consist of two arrays of hybrid Silicon Pixel Detectors (SPD) located at an average radial distance (r) of 3.9 and 7.6 cm from the beam axis and covering $|\eta| < 2$ and $|\eta| < 1.4$, respectively. The SPD is also used to reconstruct tracklets, which are track seg-

ments built using the position of the reconstructed primary vertex and two hits, one on each SPD layer. The number of tracklets gives an excellent estimate of the charged-particle multiplicity at mid-pseudorapidity (N_{ch}). The outer layers of the ITS are composed of silicon strip and drift detectors, with the outermost layer sitting at $r = 43$ cm. The TPC is a large cylindrical drift detector of radial and longitudinal size of about $85 < r < 250$ cm and $-250 < z < 250$ cm, respectively. It is segmented in radial "pad rows", providing up to 159 tracking points. The measurement of charged particles is based on "global tracks", reconstructed using the combined ITS and TPC information. The V0 detector consists of two forward scintillator arrays (V0-A and V0-C) employed for triggering, background suppression, and event-class determination. They are placed on either side of the interaction region at $z = 3.3$ m and $z = -0.9$ m, covering the pseudorapidity regions $2.8 < \eta < 5.1$ and $-3.7 < \eta < -1.7$, respectively.

The data were collected using a minimum-bias trigger which required coincident signals in both V0-A and V0-C detectors . The events were recorded in coincidence with signals from two beam pick-up counters each positioned on either side of the interaction region to tag the arrival of proton bunches from both directions. Control triggers taken for various combinations of beam and empty buckets were used to measure beam-induced and accidental backgrounds. The contamination from background events was removed offline by using the timing information from the V0 detector, which has a time resolution better than 1 ns. Background events were also rejected by exploiting the correlation between the number of clusters of pixel hits and the number of tracklets in the SPD.

3 Analysis

The results presented here were obtained from the analysis of about 105 and 60 million minimum-bias pp events at $\sqrt{s} = 5.02$ and 13 TeV, respectively. The interaction probability per single bunch crossing ranges between 2% and 14% for pp collisions at 13 TeV and from 0.3% to 6% for pp collisions at 5.02 TeV. The measurements have been obtained for events having at least one charged particle produced in the pseudorapidity interval $|\eta| < 1$ (INEL > 0). For the analysis, the events were furthermore required to have a reconstructed vertex located within $|z| < 10$ cm, where z is the position of the vertex along the beam axis, and $z = 0$ cm corresponds to the nominal center of the detector [22]. Events containing more than one distinct vertex were tagged as pileup and discarded from the analysis. The systematic uncertainty associated to pileup is between 3–4% and is not the dominant source of uncertainty for the p_T spectra reported here. The corrections are calculated using Monte Carlo events from

the PYTHIA 6 [23] (tune Perugia 2011 [24]) event generator with particle transport performed via a GEANT 3 [25] simulation of the ALICE detector.

Only primary charged particles in the kinematic range $|\eta| < 0.8$ and $0.15 < p_T < 20\,\text{GeV}/c$ are considered in the transverse momentum analysis. A primary charged particle is defined as a charged particle with a mean proper lifetime τ larger than $1\,\text{cm}/c$, which is either produced directly in the interaction or from decays of particles with τ smaller than $1\,\text{cm}/c$, excluding particles produced in interactions with the detector material [26].

Transverse momentum distributions The measurement of the p_T spectra follows the standard procedure already employed in several ALICE publications [27–29]. Tracks reconstructed using the information from the ITS and TPC detectors are used. The track selection criteria have been optimised for best track quality and minimal contamination from secondary particles. Tracks are required to have at least two hits in the ITS detector, of which at least one is in either of the two innermost SPD layers. The geometrical track length L (in cm) is calculated in the TPC readout plane, excluding the information from the pads at the sector boundaries ($\sim 3\,\text{cm}$ from the sector edges). The number of crossed TPC rows has to be larger than $0.85L$. The number of TPC clusters has to be larger than $0.7L$. The fit quality for the ITS and TPC track points must satisfy $\chi^2_{\text{ITS}}/N_{\text{hits}} < 36$ and $\chi^2_{\text{TPC}}/N_{\text{clusters}} < 4$, respectively, where N_{hits} and N_{clusters} are the numbers of hits in the ITS and the number of clusters in the TPC, respectively. Tracking information from the combined ITS and TPC track reconstruction algorithm is compared to that derived only from the TPC and constrained by the interaction vertex point. Then, the quantity $\chi^2_{\text{TPC–ITS}}$ is derived as described in Ref. [30]. Only tracks with $\chi^2_{\text{TPC–ITS}} < 36$ are included in the analysis in order to improve the purity of primary track reconstruction at high p_T. Tracks are rejected if their distance of closest approach to the reconstructed vertex in longitudinal and radial direction, d_z and d_{xy}, respectively, satisfies $d_z > 2\,\text{cm}$ or $d_{xy} > 0.018\,\text{cm} + 0.035\,\text{cm} \times p_T^{-1.01}$, with p_T in GeV/c.

Multiplicity estimators In order to study the multiplicity dependence of the inclusive charged particle p_T distributions, the INEL > 0 sample is divided into event classes based on the total charge deposited in the V0 detector (V0M amplitude) and on the number of SPD tracklets ($N_{\text{SPD tracklets}}$) in the pseudorapidity region $|\eta| < 0.8$. The event classes used in the analysis and the corresponding mid-pseudorapidity charged particle densities are summarized in Tables 1 and 2. The average charged-particle multiplicity densities for INEL > 0 collisions and for the multiplicity classes are obtained by integrating the corresponding fully corrected p_T spectra (measured using ITS and TPC information). To this end, the p_T spectra were extrapolated to $p_T = 0$ with a Hagedorn

function [31]. Different functions were used and the differences with respect to the reference values were considered in the systematic uncertainties. For INEL > 0 pp collisions at $\sqrt{s} = 5.02\,\text{TeV}$ the mid-pseudorapidity ($|\eta| < 0.8$) charged-particle density is $\langle dN_{\text{ch}}/d\eta \rangle = 5.91 \pm 0.45$, while for $\sqrt{s} = 13\,\text{TeV}$ the corresponding value is 7.60 ± 0.50. The comparison of results obtained with these estimators allows to understand potential biases from measuring the multiplicity and p_T distributions in overlapping η regions.

Spherocity For the data analysis we followed a strategy similar to that already reported in Ref. [32]. Spherocity, S_0, originally proposed here [33] is defined for a unit vector $\hat{\mathbf{n}}_\mathbf{s}$ which minimizes the ratio:

$$S_0 \equiv \frac{\pi^2}{4} \min_{\hat{\mathbf{n}}_\mathbf{s}} \left(\frac{\sum_i |\vec{p}_{T,i} \times \hat{\mathbf{n}}_\mathbf{s}|}{\sum_i p_{T,i}} \right)^2, \tag{1}$$

where the sum runs over all reconstructed ITS-TPC tracks. At least three tracks are required within $|\eta| < 0.8$ and $p_T > 0.15\,\text{GeV}/c$ in order to achieve a good spherocity resolution. The spherocity resolution improves with the track-reconstruction efficiency, therefore the restrictions on the purity of primary charged particles can be relaxed. For spherocity we considered all tracks with at least 50 clusters in the TPC, which satisfy: $d_{xy} < 2.4\,\text{cm}$, $d_z < 3.2\,\text{cm}$, and $\chi^2_{\text{TPC}}/N_{\text{clusters}} < 4$. The exclusion of the ITS requirements guarantees a homogeneous azimuthal track-reconstruction efficiency.

It is worth mentioning some important features of spherocity:

- The vector products are linear in particle momenta, therefore spherocity is a collinear safe quantity in pQCD.
- The lower limit of spherocity ($S_0 \to 0$) corresponds to event topologies where all transverse momentum vectors are (anti)parallel or the sum of the p_T is dominated by a single track.
- The upper limit of spherocity ($S_0 \to 1$) corresponds to event topologies where transverse momentum vectors are "isotropically" distributed. $S_0 = 1$ can only be reached in the limit of an infinite amount of particles.

Since the goal of the present study is to separate jet events from isotropic ones, we study different spherocity classes for a given multiplicity value. The multiplicity is measured by counting the number of tracks within $|\eta| < 0.8$. As explained later, we adopted the procedure used in the analysis of average p_T as a function of multiplicity to correct the number of tracks for detector effects [21]. The detector response is represented by a two-dimensional distribution: reconstructed spherocity as a function of generated spherocity, each bin of generated spherocity is normalized to unity. In this representation, the two-dimensional distribution gives

Table 1 V0M event multiplicity classes, their corresponding experimental definition and their corresponding $\langle \mathrm{d}N_{\mathrm{ch}}/\mathrm{d}\eta \rangle$ in $|\eta| < 0.8$. The uncertainties are the quadratic sum of statistical and systematic contributions. Statistical uncertainties are negligible compared to the systematic ones

pp collisions at $\sqrt{s} = 13$ TeV				
Class name	I	II	III	IV	V
V0M percentile	0–1%	1–5%	5–10%	10–15%	15–20%
$\langle \mathrm{d}N_{\mathrm{ch}}/\mathrm{d}\eta \rangle$	26.6±1.1	20.5±0.8	16.7±0.7	14.3±0.6	12.6±0.5
Class name	VI	VII	VIII	IX	X
V0M percentile	20–30%	30–40%	40–50%	50–70%	70–100%
$\langle \mathrm{d}N_{\mathrm{ch}}/\mathrm{d}\eta \rangle$	10.6±0.5	8.46±0.40	6.82±0.34	4.94±0.28	2.54±0.26
pp collisions at $\sqrt{s} = 5.02$ TeV				
Class name	I	II	III	IV	V
V0M percentile	0–1%	1–5%	5–10%	10–15%	15–20%
$\langle \mathrm{d}N_{\mathrm{ch}}/\mathrm{d}\eta \rangle$	19.2±0.9	15.1±0.7	12.4±0.6	10.7±0.5	9.47±0.47
Class name	VI	VII	VIII	IX	X
V0M percentile	20–30%	30–40%	40–50%	50–70%	70–100%
$\langle \mathrm{d}N_{\mathrm{ch}}/\mathrm{d}\eta \rangle$	8.04±0.42	6.56±0.37	5.39±0.32	4.05±0.27	2.27±0.27

Table 2 Event multiplicity classes based on the number of tracklets ($N_{\mathrm{SPD\,tracklets}}$) within $|\eta| < 0.8$, their corresponding experimental definition and their corresponding $\langle \mathrm{d}N_{\mathrm{ch}}/\mathrm{d}\eta \rangle$ in $|\eta| < 0.8$. The uncertainties are the quadratic sum of statistical and systematic contributions

pp collisions at $\sqrt{s} = 13$ TeV				
Class name (percentile)	I′ 0–0.006%	II′ 0.006–0.058%	III′ 0.058–0.177%	IV′ 0.177–0.513%	V′ 0.513–1.419%
$N_{\mathrm{SPD\,tracklets}}$	≥ 51	41−50	36−40	31−35	26−30
$\langle \mathrm{d}N_{\mathrm{ch}}/\mathrm{d}\eta \rangle$	54.1±2.7	44.6±2.2	38.9±1.9	34.1±1.7	29.3±1.5
Class name percentile	VI′ 1.419–3.699%	VII′ 3.699–9.059%	VIII′ 9.059–20.77%	IX′ 20.77–45.25%	X′ 45.25–100.0%
$N_{\mathrm{SPD\,tracklets}}$	21−25	16−20	11−15	6−10	0−5
$\langle \mathrm{d}N_{\mathrm{ch}}/\mathrm{d}\eta \rangle$	24.5±1.3	19.5±1.2	14.4±0.9	9.03±0.58	2.91±0.29
pp collisions at $\sqrt{s} = 5.02$ TeV				
Class name (percentile)	–	II′ 0.009–0.088%	III′ 0.088–0.253%	IV′ 0.253–0.700%	V′ 0.700–1.840%
$N_{\mathrm{SPD\,tracklets}}$	–	41−50	36−40	31−35	26−30
$\langle \mathrm{d}N_{\mathrm{ch}}/\mathrm{d}\eta \rangle$	–	34.6±1.8	29.9±1.5	26.2±1.3	22.4±1.1
Class name (percentile)	VI′ 1.840–4.573%	VII′ 4.57–10.69%	VIII′ 10.69–23.50%	IX′ 23.50–49.48%	X′ 49.48–100.0%
$N_{\mathrm{SPD\,tracklets}}$	21−25	16−20	11−15	6−10	0−5
$\langle \mathrm{d}N_{\mathrm{ch}}/\mathrm{d}\eta \rangle$	18.5±1.0	14.6±0.9	10.6±0.7	6.58±0.43	2.21±0.24

the normalized response matrix $R'(S_0, S_{\mathrm{m}})$, which contains the probability that an event with spherocity S_0 is reconstructed with spherocity S_{m}. Figure 1 shows the spherocity response matrices for two track multiplicity (N_{m}). Tracking efficiency effects on the spherocity resolution are relevant only for low-multiplicity events, therefore, the S_0 resolution improves with increasing multiplicity.

In order to study the spherocity dependence of the particle production for a given track multiplicity value, the sample is divided into ten event sub-classes of equal size (percentiles),
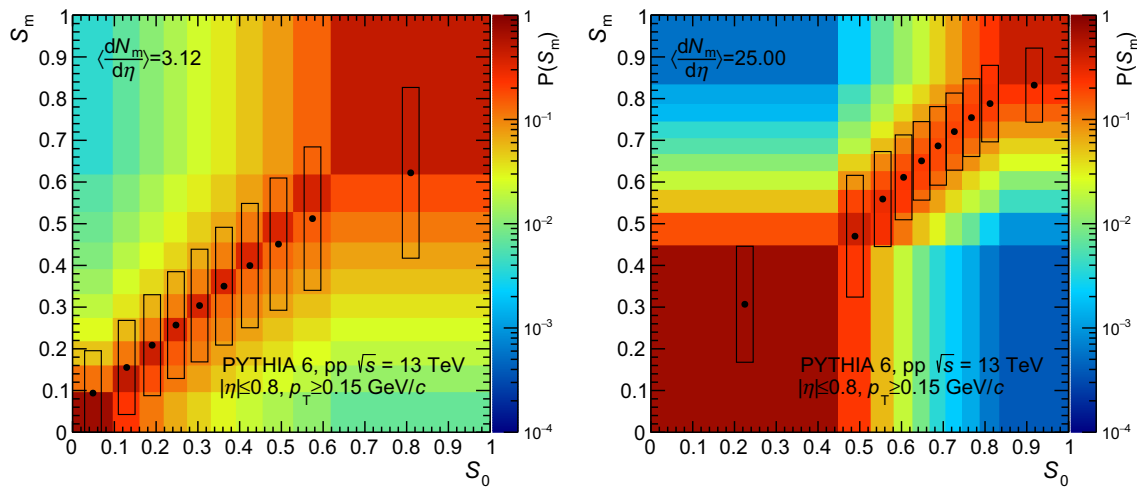
Fig. 1 The detector response for sphericity for two track multiplicity classes: $\langle dN_m/d\eta \rangle = 3.12$ (left) and $\langle dN_m/d\eta \rangle = 25$ (right). Proton-proton collisions were simulated using PYTHIA 6. The simulations include the particle transport performed via a GEANT 3 simulation of the ALICE detector. The markers (boxes around the points) indicate the average (RMS) of the measured sphericity distributions for each bin of sphericity at generator level. The sphericity binning varies with $dN_m/d\eta$, because in this way, it allows the analysis of ten event subclasses of equal size. The probability that an event with sphericity S_0 be reconstructed with sphericity S_m is represented by $P(S_m)$

based on the measured sphericity distribution. From now on, the most jet-like and isotropic events will be referred to as $0-10\%$ and $90-100\%$ sphericity event class, respectively.

It has been reported that the evolution of several observables as a function of center-of-mass energy can be factored out to be due to the changes in charged-particle multiplicities which in turn depend on the energy. For example, the particle production sensitive to the underlying event for different $\sqrt{s}$ exhibits approximate scaling properties connected to changes in $\langle N_{ch} \rangle$ [34]. Moreover, within uncertainties, the average p_T as a function of multiplicity exhibits a small energy dependence [21]. Therefore, the sphericity dependent average p_T as a function of charged-particle multiplicity is only presented for pp collisions at $\sqrt{s} = 13$ TeV. The physics message is valid for other center-of-mass energies, this was verified using data from pp collisions at $\sqrt{s} = 5.02$ TeV.

4 Corrections

All the measurements presented in this paper are fully corrected for acceptance and tracking efficiency, contamination from secondary particles, event and signal loss, as well as multiplicity and sphericity resolution. Details of these corrections are presented below.

4.1 Transverse momentum distributions as a function of particle multiplicity

The transverse momentum spectrum for a specific event class is obtained by correcting the track yields N^{rec} reconstructed in each $(\Delta\eta, \Delta p_T)$ interval for all detector effects that either

influence the event reconstruction or the track reconstruction. The transverse momentum distribution is obtained as follows:

$$\frac{1}{N_{ev}}\frac{d^2 N_{ch}}{d\eta d p_T} \equiv \frac{N^{rec}(\eta, p_T) C(\eta, p_T)}{N_{ev}^{rec} \Delta\eta \Delta p_T} \epsilon_{ev.\,class} \epsilon_{vz}. \quad (2)$$

The event selection (for a specific event class) and vertex reconstruction efficiencies are represented by $\epsilon_{ev.\,class}$ and ϵ_{vz}, respectively. The number of events of a given event class is represented by N_{ev}^{rec}. For the lowest multiplicity class selected using the V0M amplitude and for $\sqrt{s} = 5.02$ TeV ($\sqrt{s} = 13$ TeV) they reach 66% and 95% (75% and 95%), respectively, while for the highest multiplicity class the detector is fully efficient. The track-level correction factors, $C(\Delta\eta, \Delta p_T)$, are obtained for events which satisfy the selection criteria; they include acceptance, efficiency, purity, and p_T resolution. The estimation of the four terms will be explained in detail in the following.

A data-driven method has been developed to reduce the systematic uncertainty related to incorrect description of the particle composition in Monte Carlo. The tracking efficiency is determined using the re-weighting procedure which is discussed for the first time in Ref. [29] and which is employed also in the present paper. The method uses the knowledge of the particle composition at LHC energies, i.e. the abundances of the different particle species within a specific interval of p_T and for a specific event class.

To correct the distributions for secondary-particle contamination, i.e. the products of weak decays of kaons and Λ baryons, and the particles originating from interactions in the detector material, we used the d_{xy} distributions of particles in data and Monte Carlo simulations. Exploiting the differ-

ences of the d_{xy} distributions between primary and secondary particles, especially in the tails, the measured distributions were fitted by a linear combination of d_{xy} distributions (templates) for primary and secondary particles obtained from Monte Carlo simulations in different p_T bins. For INEL > 0 pp collisions at $\sqrt{s} = 13$ TeV the contamination ranges from 8.5% at $p_T = 0.2$ GeV/c to 1% for $p_T > 2$ GeV/c. The contamination exhibits a small multiplicity dependence, which is below 2%. For pp collisions at $\sqrt{s} = 5.02$ TeV, the correction factors reach similar values.

The transverse momentum spectra are also corrected for p_T resolution; the correction factor is calculated using the covariance matrix of the Kalman fit [35]. The p_T (multiplicity) dependence of the correction factor is negligible [29] (below 1%).

Finally, the p_T spectra are corrected for the amount of signal which is missing from the yield due to the event selection (signal loss). This correction is negligible for high-multiplicity events and reaches 13% (4%) at $p_T = 0.2$ ($p_T = 1$) GeV/c for the lowest multiplicity class based on $N_{SPD tracklets}$.

4.2 Spherocity studies

The measurement of the average transverse momentum as a function of charged-particle multiplicity and spherocity is performed following a strategy close to that used in earlier publications [21,36]. The transverse momentum spectra for different multiplicity and spherocity classes are fully corrected as described in the previous section. The average transverse momentum is then calculated from the corrected spectra as the arithmetic mean in the kinematic range $0.15 < p_T < 10$ GeV/c and $|\eta| < 0.8$.

To extract the correlation between $\langle p_T \rangle$ and the number of primary charged particles (N_{ch}) in $|\eta| < 0.8$ and for the spherocity class S_0, the following re-weighting procedure is applied to account for the experimental resolution of the measured event multiplicity (N_m) and spherocity (S_m):

$$\langle p_T \rangle (N_{ch}, S_0)$$
$$= \sum_{N_m} \sum_{S_m} R(N_{ch}, N_m) \langle p_T \rangle (N_m, S_m) R'(S_0, S_m). \quad (3)$$

This method is an extension to the one developed for the previous $\langle p_T \rangle$ analysis [36]. It exploits the normalized response matrices R and R' which encode the multiplicity, and spherocity detector resolutions, respectively. The average p_T for the S_0 event class is encoded inside the inner sum, where the weights $R'(S_0, S_m)$ are explicitly applied to $\langle p_T \rangle$ values. The resulting $\langle p_T \rangle (N_m, S_0)$ is then corrected for multiplicity resolution. It is worth mentioning that the spherocity-integrated class (0–100%) only requires the mul-

tiplicity correction. The Monte Carlo non-closure, discussed in the next section, is assigned as systematic uncertainty.

5 Systematic uncertainties

5.1 Transverse momentum spectra

The relative systematic uncertainties on the p_T spectra are summarized in Table 3. They include the effect of the event selection based on the vertex position, which is studied by comparing the fully corrected p_T spectra obtained with alternative vertex selections: $|z| < 5$ cm and $|z| < 20$ cm. The corrections due to trigger and vertex selection were determined using the EPOS LHC [37] event generator and the deviations with respect to the nominal values, i.e. those obtained with PYTHIA 6, were assigned as systematic uncertainties. The same procedure was employed for the estimation of the systematic uncertainty associated to the signal loss correction. The systematic uncertainty related to the track selection was studied by varying the track cuts for which we used the variation intervals described in Ref. [29]. We also studied the systematic effects related to the uncertainty on the primary particle composition which is assumed for the efficiency correction. This uncertainty takes into account the extrapolation of the spectra to low p_T, the relative particle abundances at high p_T, the uncertainties of the measured particle spectra, and the Monte Carlo assumptions on the $\Sigma^\pm / \Lambda$ spectra ratios. The systematic uncertainties of the correction for secondaries contamination is estimated by varying the fit model using two templates, i.e. for primaries and secondaries, or three templates, i.e. primaries, secondaries from interactions in the detector material, and secondaries from weak decays, as well as varying the fit momentum ranges. Since we are using the same event selection and track cuts as those used in Ref. [29], the systematic uncertainties associated with matching efficiency, p_T resolution and material budget, are identical.

5.2 Average transverse momentum

A summary of the systematic uncertainties for three multiplicity values and for different spherocity classes is shown in Table 4. In order to estimate the systematic uncertainties of $\langle p_T \rangle$, the results of the data analysis and of the evaluation of the corrections from Monte Carlo simulations were studied considering cut variations and Monte Carlo assumptions, within reasonable limits. The effect of the track cuts on $\langle p_T \rangle$ was found to be spherocity independent and of the order of 1%. The efficiency correction is another spherocity independent contribution and it is found to be ∼1%. This contribution takes into account the different particle composition in data and models, as well as the multiplicity dependence of

Table 3 Main sources and values of the relative systematic uncertainties of transverse momentum spectra for pp collisions at $\sqrt{s} = 5.02$ TeV. The maximum values of the uncertainties, among all the multiplicity classes, are reported for low-, intermediate-, and high-p_T intervals. Systematic uncertainties for pp collisions at $\sqrt{s} = 13$ TeV are shown inside the parentheses. The systematic uncertainty due to trigger and event selection is p_T independent and therefore it is not included in the table. It reaches $\sim 7.6\%$ ($\sim 6.3\%$) for the lowest multiplicity class in pp collisions at $\sqrt{s} = 5.02$ TeV ($\sqrt{s} = 13$ TeV), and it is smaller than 0.5% for the other multiplicity classes

pp collisions at $\sqrt{s} = 5.02$ TeV ($\sqrt{s} = 13$ TeV)			
p_T (GeV/c)	0.15	3.0	10
Pileup	3.5% (3.5%)	4.5% (4.5%)	4.5% (4.5%)
Vertex selection	0.5% (0.5%)	0.5% (0.5%)	0.5% (0.5%)
Signal loss	2.3% (1.1%)	1.2%(0.5%)	0.4% (0.7%)
Track selection	1.6% (1.7%)	3.1% (1.7%)	4.0% (4.0%)
Secondary particles	1.3% (1.4%)	1.0% (1.0%)	1.0% (1.0%)
Particle composition	2.0% (2.0%)	2.5% (2.5%)	2.0% (2.0%)
Tracking efficiency	1.0% (1.0%)	4.2% (4.2%)	4.2% (4.2%)
p_T resolution	0.0% (0.0%)	0.0% (0.0%)	0.1% (0.1%)
Material budget	1.5% (1.5%)	0.5% (0.5%)	0.2% (0.2%)
Total	5.4% (5.1%)	7.5% (7.0%)	7.7% (7.7%)
Total (N_{ch}-dependent)	4.1% (3.5%)	5.8% (5.5%)	5.9% (6.5%)

Table 4 Main sources and values of the relative systematic uncertainties on the average p_T for different spherocity classes. The three quoted values (for each contribution) correspond to $dN_{ch}/d\eta = 1.88$, 6.25, and 25.0, respectively

Spherocity class	0–100%	0–10%	40–50%	90–100%
Spherocity-dependent contributions				
Model dep. (%)	0.5, 0.7, 0.2	0.4, 0.4, 0.6	0.6, 0.5, 0.3	0.9, 0.8, 0.2
Sec. particles (%)	0.2, 0.3, 1.2	1.0, 1.5, 1.9	0.3, 0.3, 1.1	0.6, 0.3, 0.9
Ev. selection (%)	2.2, 0.0, 0.0	1.9, 1.4, 0.4	1.3, 0.4, 0.0	1.3, 0.1, 0.00
S_o res. corr. (%)	na	3.2, 5.4, 0.6	4.6, 2.4, 1.1	7.1, 3.7, 2.0
S_o track cuts (%)		1.00		
Spherocity-independent contributions				
N_{ch} res. corr (%)	1.4, 0.9, 1.3			
p_T track cuts (%)	0.8, 0.9, 1.2			
Efficiency corr. (%)	0.4, 0.2, 0.2			
Particle composition (%)	1.0, 1.0, 1.0			
N_{ch} dep. eff. corr. (%)	0.5, 0.7, 0.9			
N_{ch} dep. sec. corr. (%)	0.2, 0.1, 0.1			
S_o-dep. total (%)	2.2, 0.8, 1.2	4.0, 5.8, 2.3	4.9, 2.7, 1.9	7.3, 3.9, 2.4
S_o-indep. total (%)	2.0, 1.8, 2.2			
Total (%)	3.0, 2.0, 2.5	4.5, 6.1, 3.2	5.3, 3.2, 3.0	7.6, 4.3, 3.3

the correction. We also studied the multiplicity dependence of the purity correction; the effect was found to be smaller than 0.5%. The most relevant spherocity independent contribution is related to the re-weighting procedure to correct for the detector multiplicity resolution. This was quantified from the Monte Carlo non-closure, it amounts to $\sim 1.36\%$, $\sim 0.86\%$ and $\sim 1.26\%$ for $dN_{ch}/d\eta = 1.88$, 6.25, 25.00, respectively.

The set of track cuts used to measure spherocity was also varied compared to those used for the p_T spectra analysis. The effect on the results amounted to 1%. The most

relevant contribution to the systematic uncertainties originates from the re-weighting procedure method which is used to correct for the spherocity resolution. The Monte Carlo non-closure is assigned as a systematic uncertainty. For the lowest multiplicity value, $dN_{ch}/d\eta = 1.88$, the uncertainty reaches 3.23%, 4.55%, and 7.06% for the 0–10%, 40–50%, and 90–100% spherocity classes, respectively. For higher multiplicities, e.g. $dN_{ch}/d\eta = 25.0$, the Monte Carlo non-closure amounts to 0.57%, 1.07%, and 2.01% for the 0–10%, 40–50%, and 90–100% spherocity classes, respec-

tively. As expected from the detector response, the most relevant effects are observed for low-multiplicity events in particular for the isotropic classes. As will be seen later, in Monte Carlo jet-like events, the average p_T shows a strong change with multiplicity at $dN_{ch}/d\eta \sim 7$. This effect increases the size of the uncertainty (Monte Carlo non-closure) in that multiplicity interval. This is the dominant contribution to the systematic uncertainties and covers the largest variations observed between data and PYTHIA 8 (version 8.212) [10] (tune Monash 2013 [38]).

The model dependence is also checked by using events simulated with PYTHIA 8 and EPOS LHC which include the particle transport through the detector. The corrections were calculated using these simulations and the maximum variation with respect to the nominal values (using PYTHIA 6 simulations) are below 1%.

6 Results

6.1 Transverse momentum spectra as a function of charged-particle multiplicity

The p_T distributions of charged particles, measured in $|\eta| <$ 0.8 for pp collisions at $\sqrt{s} = 5.02$ and 13 TeV, are shown in Fig. 2 for the different multiplicity classes selected using the estimator based on $N_{SPD\ tracklets}$. The bottom panels depict the ratios to the p_T distribution of the INEL > 0 event class. The features of the spectra, i.e. the change of the spectral shape going from low- to high-multiplicity values, are qualitatively the same for both energies. The only significant difference is the multiplicity reach which is higher at 13 TeV than that at 5.02 TeV. In the following we discuss the results for pp collisions at the highest energy. As shown in Fig. 2, the p_T spectra become harder as the multiplicity increases, which contributes to the increase of the average transverse momentum with multiplicity. The ratios to the INEL> 0 p_T distribution exhibit two distinct behavior. While at low p_T (< 0.5 GeV/c) the ratios exhibit a modest p_T dependence, for $p_T > 0.5$ GeV/c they strongly depend on multiplicity and p_T.

Figure 3 shows the multiplicity dependent p_T spectra using a multiplicity selection based on the V0M amplitude. Results for pp collisions at $\sqrt{s} = 5.02$ and 13 TeV are shown. The average multiplicity values are significantly smaller than those reached with the mid-pseudorapidity estimator (based on $N_{SPD\ tracklets}$). For example, in pp collisions at $\sqrt{s} = 13$ TeV, while the average charged-particle multiplicity density amounts to 56.55 for the highest $N_{SPD\ tracklets}$ class, it only reaches 27.61 for the highest V0M multiplicity class. We note that for similar average particle densities, e.g. the multiplicity classes II (V0M) and VII' (SPD tracklets) in pp collisions at $\sqrt{s} = 13$ TeV, the ratios measured using
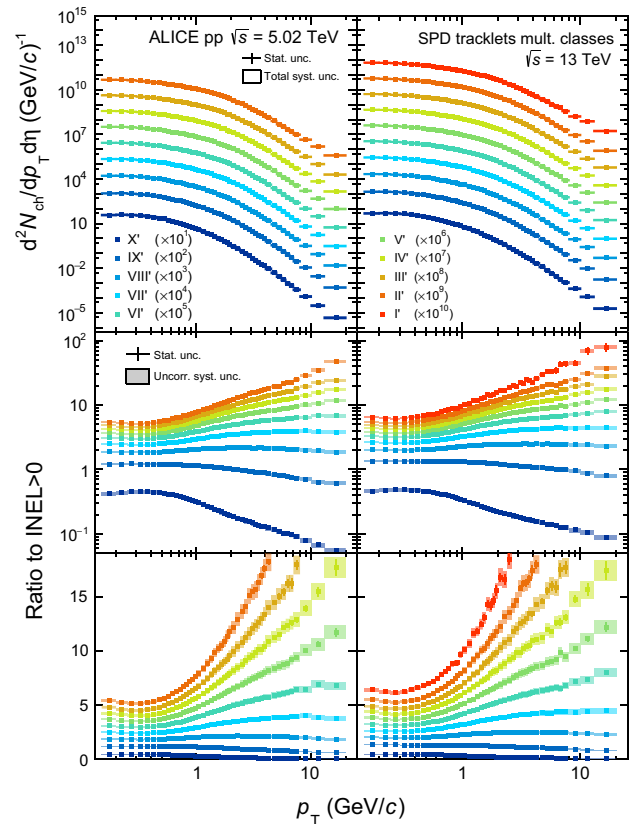

Fig. 2 Transverse momentum distributions of charged particles for multiplicity classes selected using SPD tracklets in $|\eta| < 0.8$. Results for pp collisions at $\sqrt{s} = 5.02$ and 13 TeV are shown in the left and right panels, respectively. Statistical and total systematic uncertainties are shown as error bars and boxes around the data points, respectively. In the middle panels, ratios of multiplicity dependent spectra to INEL > 0 are shown in logarithmic scale. In the bottom panels we show the ratios in a linear scale to illustrate the dramatic behavior of the ratios. The systematic uncertainties on the ratios are obtained by considering only contributions uncorrelated across multiplicity. The spectra are scaled to improve the visibility

the V0M amplitude and the $N_{SPD\ tracklets}$ are similar. The comparison of the p_T spectra for these multiplicity classes is shown in Fig. 4. We observe that for transverse momentum below 0.5 GeV/c, the spectra exhibit the same shape. For transverse momenta within 0.5–3 GeV/c the spectra for the multiplicity class II is harder than that for the VII'' class. At higher p_T, the spectral shapes are the same, but the yield of the class II is ∼15% higher than that for the VII' class. Similar results are obtained if we compare the multiplicity classes I and VI' for pp collisions at 5.02 TeV.

Commonly, the particle production is characterized by quantities like integrated yields, or any fit parameter of the curve extracted from fits to the data, for example, the so-called inverse slope parameter reported by ALICE in Ref. [39]. This facilitates the visualization of the evolution of the particle production as a function of multiplicity and the com-
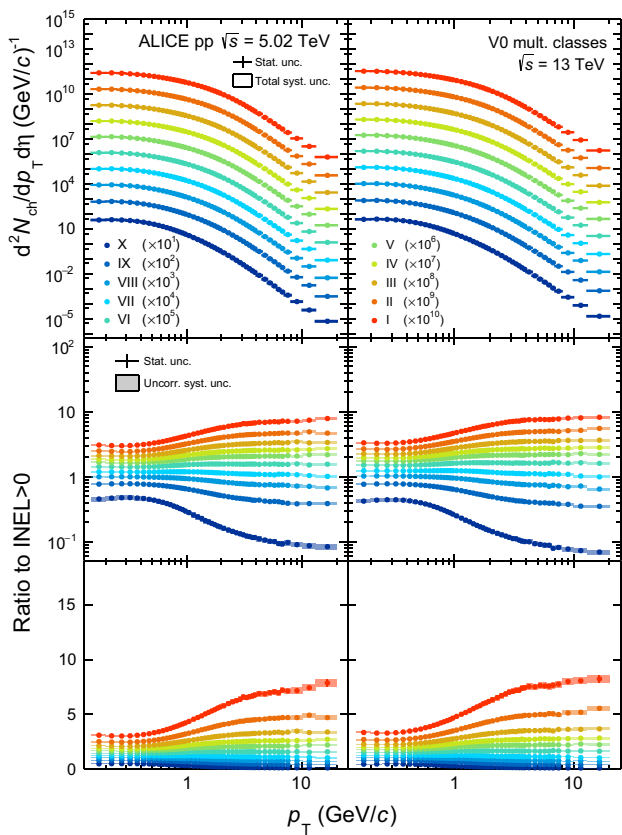
Fig. 3 Transverse momentum distributions of charged particles for different V0M multiplicity classes. Results for pp collisions at $\sqrt{s} = 5.02$ and 13 TeV are shown in the left and right panels, respectively. Statistical and total systematic uncertainties are shown as error bars and boxes around the data points, respectively. In the middle panels, ratios of multiplicity dependent spectra to INEL > 0 are shown in logarithmic scale. The systematic uncertainties on the ratios are obtained by considering only contributions uncorrelated across multiplicity. The spectra are scaled to improve the visibility

Fig. 4 Transverse momentum distributions of charged particles for high-multiplicity ($\langle dN_{ch}/d\eta \rangle \approx 20$) pp collisions at $\sqrt{s} = 5.02$ (empty markers) and 13 TeV (full markers). Results for V0-based (squares) and SPD-based (circles) multiplicity estimators are shown. The bottom panel shows the p_T spectrum obtained using the V0-based multiplicity estimator normalized to that using the SPD-based multiplicity estimator. Only statistical uncertainties are shown as error bars

parison among different colliding systems. Several publications have adopted this strategy for soft ($p_T < 2$ GeV/c) [2,6,21] physics and others to describe the particle production for intermediate and high p_T ($2 \leq p_T < 20$ GeV/c) [40]. It is interesting and important to define a common quantity to compare the shape of the high-p_T part of the spectra of different particle species and collision systems. The natural choice is fitting a power-law function ($\alpha \times p_T^{-n}$) to the invariant yield and studying the multiplicity dependence of the exponent (n) extracted from the fit. Figure 5 illustrates the results considering particles with transverse momentum within 6–20 GeV/c for pp at $\sqrt{s} = 13$ TeV. It is worth mentioning that within uncertainties the power-law function describes rather well the data in that p_T interval. Similarly, the p_T spectra simulated with the different generators are well described (within 2%) by the power-law function.

Within uncertainties, going from low to high multiplicity n decreases taking values from 6 to 5, respectively.

A similar behavior has been reported for heavy-ion collisions [41]. Moreover, the results using the two multiplicity estimators are consistent within the overlapping multiplicity interval. This result is consistent with that shown in Fig. 4. PYTHIA 6 and 8 simulations describe the trends very well, but a strong deviation between EPOS LHC and data is observed. In PYTHIA 8, it has been shown that the number of high-p_T jets increases with event multiplicity. Moreover, for a given event multiplicity and fixed jet p_T, the high-p_T tails of the charged-particle spectra are very similar in low- and high-multiplicity events [16]. Therefore, based on PYTHIA 8 studies, the reduction of the power-law exponent with increasing multiplicity can be attributed to an increasing number of high-p_T jets.

As pointed out above, the ratios to the INEL > 0 p_T distributions for $\langle dN_{ch}/d\eta \rangle \lesssim 25$ exhibit a weak p_T-dependence for $p_T > 4$ GeV/c. This applies to both energies and to all multiplicity estimators. To illustrate better the behaviour of the yields at high momenta, we adopted a representation previously used for heavy-flavour hadrons [42] to point out to the similarities between the two results. The trend at high-p_T is highlighted in Fig. 6, which shows the integrated yields for three transverse momentum intervals ($2 < p_T < 10$ GeV/c, $4 < p_T < 10$ GeV/c, and $6 < p_T < 10$ GeV/c) as a func-
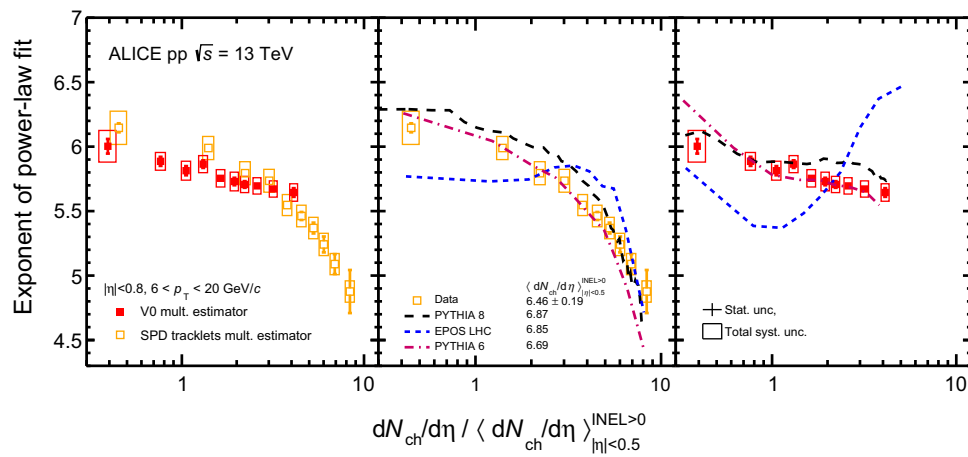
Fig. 5 Evolution of the spectral shape of the transverse momentum distribution as a function of charged-particle multiplicity. The spectral shape is characterized by the exponent of the power-law function which fits the high-p_T part ($p_T > 6\,\mathrm{GeV}/c$) of the invariant yields. Results for pp collisions at $\sqrt{s} = 13\,\mathrm{TeV}$ are shown. A comparison of the two mul-tiplicity estimators discussed in this paper is shown in the left panel. Comparisons with Monte Carlo generators predictions are shown in the middle and right panels. Statistical and total systematic uncertainties are shown as error bars and boxes around the data points, respectively
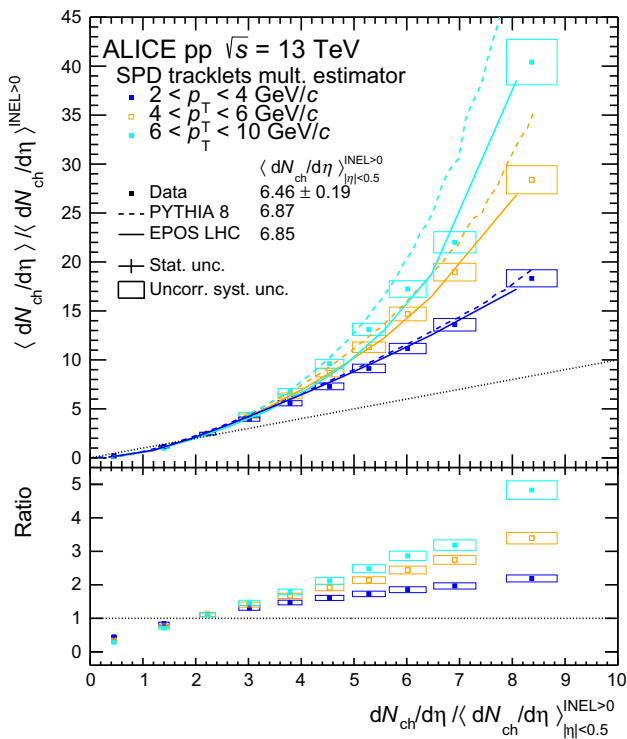
Fig. 6 Self-normalized yields of charged particles integrated over different p_T intervals: $2 < p_T < 4\,\mathrm{GeV}/c$, $4 < p_T < 6\,\mathrm{GeV}/c$, and $6 < p_T < 10\,\mathrm{GeV}/c$. The integrated yields for pp collisions at $\sqrt{s} = 13\,\mathrm{TeV}$ are shown as a function of charged-particle density at mid-pseudorapidity. Statistical and uncorrelated (across multiplicity) systematic uncertainties are shown as error bars and boxes around the data points, respectively. Statistical uncertainties are negligible compared to systematic uncertainties. Data are compared with PYTHIA 8 (dashed lines) and EPOS LHC (solid lines). The dotted line is drawn to see the differences between data and the linear dependence. Deviations of data from the linear trend are shown in the bottom panel

tion of the average mid-pseudorapidity multiplicity. Both the charged-particle yields and the average multiplicity are self-normalized, i.e. they are divided by their average value for the INEL > 0 sample. The high-p_T ($> 4\,\mathrm{GeV}/c$) yields of charged particles increase faster than the charged-particle multiplicity, while the increase is smaller when we consider lower-p_T particles. The trend of the data is qualitatively well reproduced by PYTHIA 8, but for $p_T > 6\,\mathrm{GeV}/c$ the model significantly overestimates the ratio by a factor larger than 1.5. Although the shapes of the spectra (characterized by n) are not well reproduced by EPOS LHC, the model gives the best description of the self-normalized yields. Despite the large uncertainties, it is clear the data show a non-linear increase.

6.2 Double-differential study of the average transverse momentum

The sphericity-integrated average p_T as a function of $\mathrm{d}N_{ch}/\mathrm{d}\eta$ for pp collisions at $\sqrt{s} = 13\,\mathrm{TeV}$ is shown in Fig. 7. In accordance with measurements at lower energies [21], the $\langle p_T \rangle$ increases with $\mathrm{d}N_{ch}/\mathrm{d}\eta$. In PYTHIA 8 the effect is enhanced by color reconnection, which allows the interaction among partons originating from multiple semi-hard scatterings via color strings. The minimum-bias data are compared with analogous measurements for the most jet-like structure (0–10%) and isotropic (90–100%) event classes. Studying observables as a function of sphericity reveals interesting features. On one hand, for isotropic events the average p_T stays systematically below the sphericity-integrated $\langle p_T \rangle$ over the full multiplicity range; on the other hand, for jet-like events the $\langle p_T \rangle$ is higher than that for sphericity-integrated
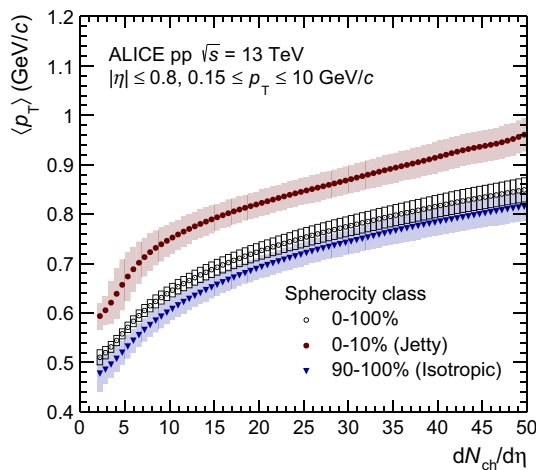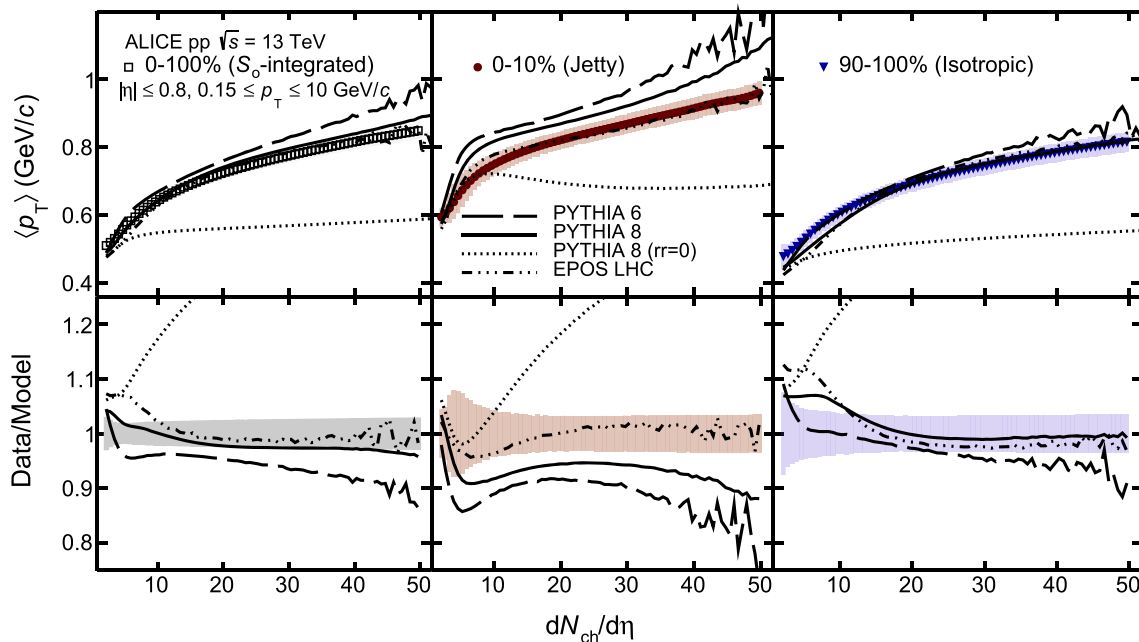
Fig. 7 Average transverse momentum as a function of event multiplicity in pp collisions at $\sqrt{s} = 13$ TeV. Results for the spherocity-integrated case (0–100%) are contrasted with the measurements for the most jet-like (0–10%) and isotropic (90–100%) events. Statistical uncertainties (error bars) are negligible compared to systematic uncertainties (boxes around the data points)

events. Moreover, within uncertainties the overall shape of the correlation, i.e. a steep linear rise below $\mathrm{d}N_{\mathrm{ch}}/\mathrm{d}\eta = 10$ followed by a less steep but still linear rise above, is not spherocity-dependent.

Figure 8 shows that within uncertainties, PYTHIA 8 with color reconnection gives an adequate description of the spherocity-integrated event class. It is worth mentioning that color reconnection was originally introduced to explain the rise of $\langle p_{\mathrm{T}} \rangle$ with multiplicity [43]. However, PYTHIA 6 shows a steeper rise of $\langle p_{\mathrm{T}} \rangle$ with $\mathrm{d}N_{\mathrm{ch}}/\mathrm{d}\eta$ than that seen in data. The Perugia 2011 tune relies on Tevatron and SPS minimum-bias data, while the Monash tune was constrained using the early LHC measurements [38]. The comparison of data with EPOS LHC is also shown. Clearly, the quantitative agreement is as good as that achieved by PYTHIA 8. The EPOS LHC model uses a different approach in order to simulate the hadronic interactions. Namely, the model considers a collective hadronization which depends only on the geometry and the density [37].

For the 0–10% and 90–100% spherocity classes, Fig. 8 also shows comparisons between data and Monte Carlo generators (PYTHIA 6, PYTHIA 8 and EPOS LHC). It is worth mentioning that we also used spherocity percentiles in all the Monte Carlo event generators reported in this paper because their spherocity distributions do not differ much from those measured in data. For further Monte Carlo comparisons the spherocity binning which was used in the analysis is provided as HEP data. In low-multiplicity events ($\mathrm{d}N_{\mathrm{ch}}/\mathrm{d}\eta < 10$), the deviations between data and PYTHIA 8 (without color reconnection) are smaller and larger respectively for the 0–

Fig. 8 Average transverse momentum as a function of event multiplicity in pp collisions at $\sqrt{s} = 13$ TeV. Results for the spherocity-integrated case (0–100%), the most jet-like (0–10%) and isotropic (90–100%) events are compared with Monte Carlo predictions. Predictions of PYTHIA 8 with and without (null reconnection range, rr = 0) color reconnection, as well as PYTHIA 6 and EPOS LHC are displayed. Statistical uncertainties (error bars) are negligible compared to systematic uncertainties (shaded area around the data points). Data to model ratios are shown in the bottom panel. The color band around unity represents the systematic uncertainty

10% and 90–100% spherocity classes than those seen for the 0–100% spherocity class. The effect could be a consequence of the reduction of color reconnection contribution in events containing jets surrounded by a small underlying event activity. For isotropic events the three models quantitatively describe the correlation. Even for PYTHIA 6, the size of the discrepancy which was pointed out for the spherocity-integrated event class is reduced. On the contrary, for jet-like events both PYTHIA 6 and 8 exhibit a larger disagreement with the data. These models produce three distinct multiplicity regions, for $dN_{ch}/d\eta \lesssim 7$ the models give a steeper rise of $\langle p_T \rangle$ than data. Within the intermediate multiplicity interval ($7 \lesssim dN_{ch}/d\eta \lesssim 25$), the slope of $\langle p_T \rangle$ given by models is more compatible with that seen in data, although the models overestimate the average p_T. While in data the average p_T increases at a constant rate with multiplicity for $dN_{ch}/d\eta \gtrsim 7$, PYTHIA 6 and 8 shows a third change of the slope of $\langle p_T \rangle$, observed for $dN_{ch}/d\eta \gtrsim 25$. The data to model ratio indicates a discrepancy larger than 10%, which is larger than the systematic uncertainties associated to $\langle p_T \rangle$ in that multiplicity interval.

In order to study the details of the changes of the functional form of $\langle p_T \rangle(N_{ch})$ due to the spherocity selection, Fig. 9 shows the average p_T of jet-like and isotropic events normalized to that for the spherocity-integrated event class. For jet-like events, the data exhibit a hint of a modest peak at $dN_{ch}/d\eta \sim 7$, which is not significant if we consider the size of the systematic uncertainties. Moreover, within uncertainties the ratio remains constant for $dN_{ch}/d\eta \gtrsim 25$. EPOS LHC describes rather well the high-multiplicity behavior, however, it overestimates the peak. PYTHIA 6 and 8 show the worst agreement with the data. In this representation, the three distinct regions, which were described before are highlighted. In PYTHIA 8, the peak (at $dN_{ch}/d\eta \sim 7$) in jet-like events is caused by particles with transverse momentum above 2 GeV/c. The size of the peak is determined by particles with $p_T > 5 - 6$ GeV/c. In contrast, data do not show a significant peak structure for any specific transverse momentum interval. We also varied the upper p_T ($0.15 < p_T < p_T^{max}$) limit ($p_T^{max} = 10$ GeV/c is the default) and studied the effect on the extracted $\langle p_T \rangle$. The $\langle p_T \rangle$ remains constant within uncertainties for $4 < p_T^{max} < 10$ GeV/c in data and for $6 < p_T^{max} < 10$ GeV/c in PYTHIA 8. For $p_T^{max} = 2$ GeV/c the $\langle p_T \rangle$ decreases by 23% (29%) in data (PYTHIA 8) compared to $p_T^{max} = 10$ GeV/c. The relative difference of $\langle p_T \rangle$ between data and PYTHIA 8 amounts to 9% (4%) for $p_T^{max} = 2$ GeV/c ($p_T^{max} = 10$ GeV/c). The results suggest that the power-law tail produces a smaller impact on data than in PYTHIA 8. A similar ratio for isotropic events shows a smaller structure at $dN_{ch}/d\eta \sim 7$. This effect is well reproduced by all models.

Finally, we also examined the evolution of $\langle p_T \rangle(N_{ch})$ going from the most jet-like to the most isotropic event

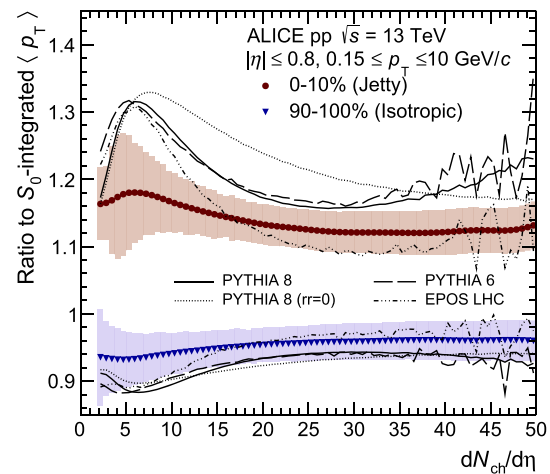**Fig. 9** Average p_T of jet-like (circles) and isotropic (triangles) events normalized to that for the spherocity-integrated event class. The measurements are compared with different Monte Carlo generators. Statistical uncertainties (error bars) are negligible compared to systematic uncertainties (boxes around the data points)

classes. Figure 10 shows the spherocity-dependent $\langle p_T \rangle(N_{ch})$ in data and models, the data to model ratios are displayed in Fig. 11. The difference between the 0–10% and 10–20% spherocity classes is smaller for data and EPOS LHC than for PYTHIA 6 and 8. Moreover, within uncertainties PYTHIA 8 describes rather well the data for the 10–20% spherocity class. This contrasts with the disagreement between the model and data for the 0–10% spherocity class. Other features in PYTHIA 6 and 8 are the reduction of the bump at $dN_{ch}/d\eta \sim 7$ and the disappearance of a third rise of the $\langle p_T \rangle$ for $dN_{ch}/d\eta \gtrsim 25$ when one goes from the 0–10% to the 10–20% spherocity classes. The agreement among models and data for the 20–100% spherocity classes is similar to that observed for the 10–20% spherocity class. Within uncertainties, PYTHIA 8 and EPOS LHC qualitatively describe the data for $dN_{ch}/d\eta \gtrsim 10$, while PYTHIA 6 overestimates the average p_T.

From previous LHC studies we know that the production cross section of jets in high-multiplicity pp collisions is smaller in data than predicted from the Monte Carlo generators [32,44,45]. Therefore, a possible interpretation is that the low-momentum partons, color connected with higher momentum ones (jets), would produce an overall increase of the hadron transverse momentum. This would affect more the low-p_T part of the spectrum associated with jet-enriched samples, which are achieved by requiring low-spherocity values. The incorporation of these new observables into the PYTHIA 8 tuning could be a challenge because, on one hand, the color reconnection has to be reduced to describe the low-S_0 data; on the other hand, the variation should not be too large because the good description of the spherocity-integrated and isotropic classes could be affected.
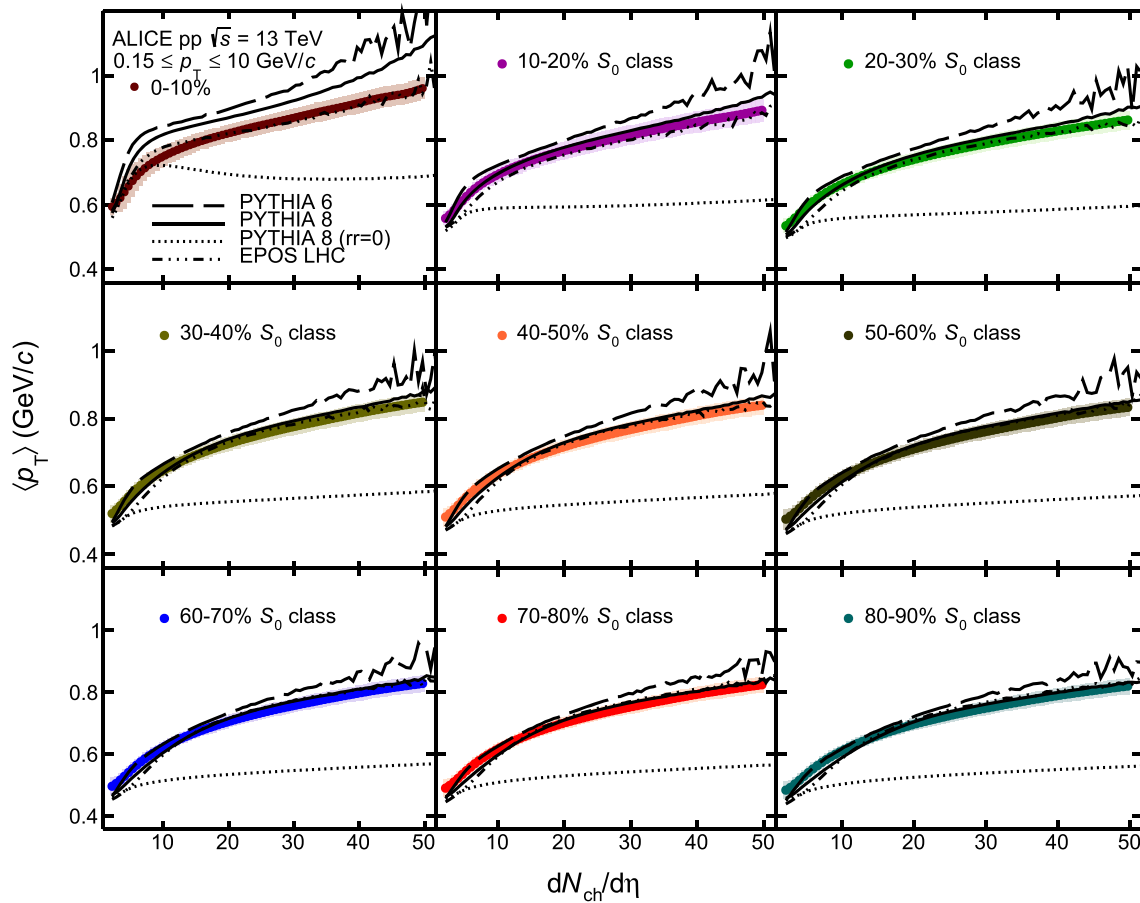
Fig. 10 Average transverse momentum as a function of event multiplicity in pp collisions at $\sqrt{s}$ = 13 TeV. Results for nine spherocity classes are compared with Monte Carlo predictions. Statistical uncertainties (error bars) are negligible compared to systematic uncertainties (shaded area around the data points)

7 Summary and conclusions

In this paper, we have reported the transverse momentum spectra of inclusive charged particles in pp collisions at $\sqrt{s}$ = 5.02 and 13 TeV. The measurements were performed in the kinematic range of $|\eta| < 0.8$ and $p_T > 0.15$ GeV/c. The particle production was studied as a function of event multiplicity quantified by two estimators, one based on the number of SPD tracklets within $|\eta| < 0.8$, and the second one based on the multiplicity in the V0 forward detector (V0M amplitude). For similar average charged-particle densities, the particle production above $p_T = 1$ GeV/c is higher in pp collisions at $\sqrt{s}$ = 13 TeV than at $\sqrt{s}$ = 5.02 TeV. For a fixed center-of-mass energy, particle production above $p_T = 0.5$ GeV/c exhibits a remarkable multiplicity dependence. Namely, for transverse momenta below 0.5 GeV/c, the ratio of the multiplicity dependent spectra to those for INEL > 0 pp collisions is rather constant, and for higher momenta, it shows a significant p_T dependence. The behavior observed for each of the two multiplicity estimators

are consistent within the $\langle dN_{ch}/d\eta \rangle$ interval defined by the V0M multiplicity estimator, which gives a $\langle dN_{ch}/d\eta \rangle$ reach of ~25. For the highest V0M multiplicity class, the ratio increases going from $p_T = 0.5$ GeV/c up to $p_T \approx 4$ GeV/c, then for higher p_T, it shows a smaller increase.

The particle production at high transverse momenta is characterized by the exponent of a power-law function which is fitted to the invariant yield considering particles with $6 < p_T < 20$ GeV/c. Within that p_T interval, the power-law function describes rather well the p_T spectra. In concordance to the ratios discussed above, within uncertainties, the functional form of n as a function of $\langle dN_{ch}/d\eta \rangle$ is the same for the two multiplicity estimators used in this analysis. Moreover, n is found to decrease with $\langle dN_{ch}/d\eta \rangle$. Within uncertainties, PYTHIA 8 (tune Monash 2013) and PYTHIA 6 (tune Perugia 2011) quantitatively reproduce the behavior of data, while EPOS LHC overestimates the value of the exponent. Nevertheless, all models describe the self-normalized high-p_T yields as a function of self-normalized charged-particle multiplicity.
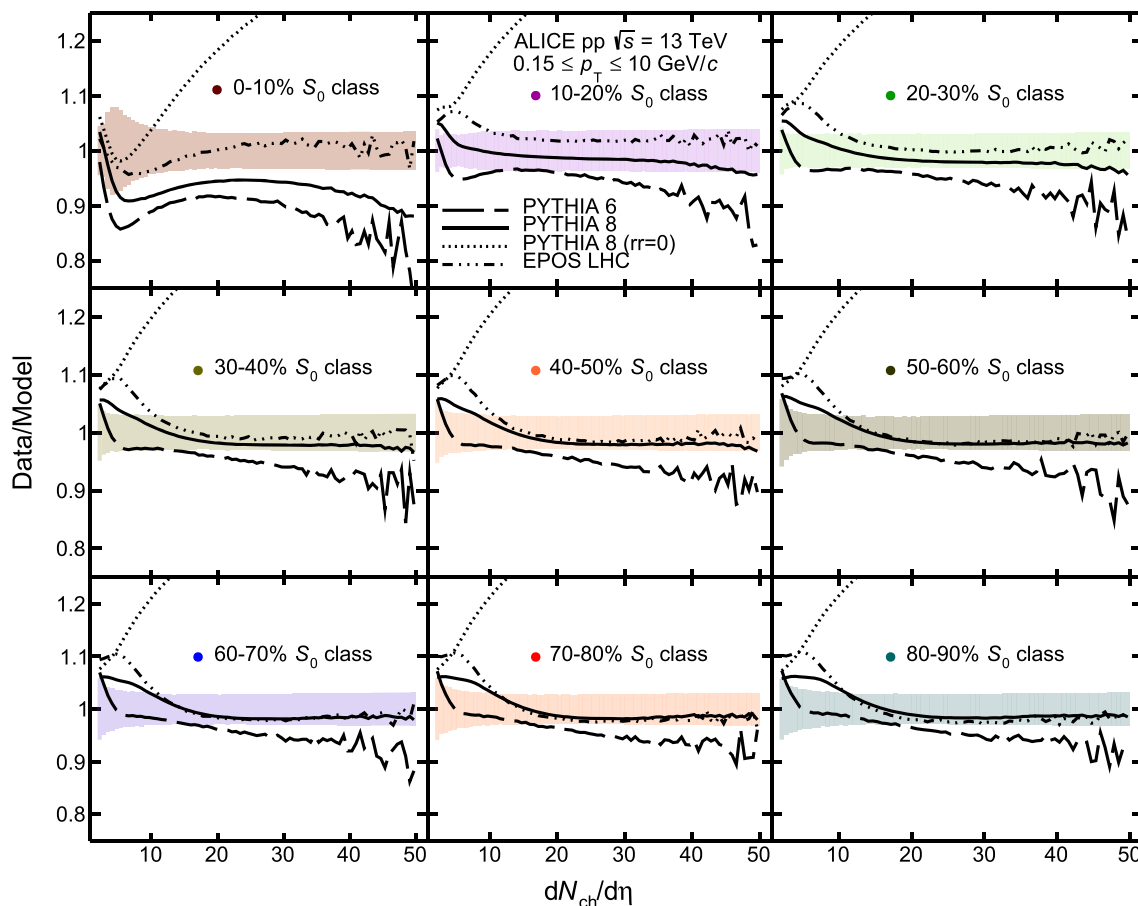
Fig. 11 Data to model ratios as a function of event multiplicity in pp collisions at $\sqrt{s} = 13$ TeV. Results for nine spherocity classes are shown. Systematic uncertainties are displayed as shaded areas around unity

Finally, the measurement of the average transverse momentum as a function of event multiplicity at mid-pseudorapidity was presented. The results for the spherocity-integrated class (nearly identical to INEL > 0 pp collisions) at $\sqrt{s} = 13$ TeV are consistent with previous measurements at lower energies. The increase of the average p_T with increasing multiplicity is well captured by PYTHIA 8 and EPOS LHC. In order to get a better insight into the particle production mechanisms, the spherocity-integrated sample was separated into different sub-classes characterized by the event structure in the transverse plane. Jet-like and isotropic events were selected based on the spherocity of the events. Isotropic events are well described by the three models which were considered in this work. Interestingly, PYTHIA 6 reproduces these event classes better than the INEL > 0 sample. For jet-like events, the average p_T is over-estimated by PYTHIA 6 and 8 models in the full multiplicity interval reported. However, EPOS LHC gives the best description of the jet-like event subsample.

The results presented in this paper illustrate the difficulties for the models to describe different observables once they

are differentially analyzed as a function of several variables. The measurements are important to better understand the similarities between heavy-ion and small collision systems, as well as for Monte Carlo tuning purposes.

References

1. C. Loizides, Experimental overview on small collision systems at the LHC. Nucl. Phys. A **956**, 200–207 (2016). arXiv:1602.09138 [nucl-ex]

2. ALICE Collaboration, B. Abelev et al., Multiplicity Dependence of Pion, Kaon, Proton and Lambda Production in p-Pb Collisions at $\sqrt{s_{NN}}$ = 5.02 TeV. Phys. Lett. B **728**, 25–38 (2014). arXiv:1307.6796 [nucl-ex]

3. ALICE Collaboration, J. Adam et al., Multiplicity dependence of charged pion, kaon, and (anti)proton production at large transverse momentum in p-Pb collisions at $\sqrt{s_{NN}}$ = 5.02 TeV. Phys. Lett. B **760**, 720–735 (2016). arXiv:1601.03658 [nucl-ex]

4. ALICE Collaboration, S. Acharya et al., Multiplicity dependence of light-flavor hadron production in pp collisions at $\sqrt{s}$ = 7 TeV. Phys. Rev. C **99**, 024906 (2019). https://doi.org/10.1103/PhysRevC.99.024906

5. CMS Collaboration, V. Khachatryan et al., Evidence for collectivity in pp collisions at the LHC. Phys. Lett. B **765**, 193–220 (2017). arXiv:1606.06198 [nucl-ex]

6. ALICE Collaboration, J. Adam et al., Enhanced production of multi-strange hadrons in high-multiplicity proton-proton collisions. Nature Phys. **13**, 535–539 (2017). arXiv:1606.07424 [nucl-ex]

7. K. Werner, M. Bleicher, B. Guiot, I. Karpenko, T. Pierog, Evidence for Flow from Hydrodynamic Simulations of p-Pb Collisions at 5.02 TeV from v_2 Mass Splitting. Phys. Rev. Lett. **112**(23), 232301 (2014). arXiv:1307.4379 [nucl-th]

8. C. Bierlich, G. Gustafson, L. Lönnblad, A. Tarasov, Effects of Overlapping Strings in pp Collisions. JHEP **1503**, 148 (2015). arXiv:1412.6259 [hep-ph]

9. I. Bautista, A.F. Téllez, P. Ghosh, Indication of change of phase in high-multiplicity proton-proton events at LHC in String Percolation Model. Phys. Rev. D **92**(7), 071504 (2015). arXiv:1509.02278 [nucl-th]

10. T. Sjöstrand, S. Ask, J.R. Christiansen, R. Corke, N. Desai et al., An Introduction to PYTHIA 8.2. Comput. Phys. Commun. **191**, 159–177 (2015). arXiv:1410.3012 [hep-ph]

11. A. Ortiz, P. Christiansen, E. Cuautle, I. A. Maldonado, and G. Paić, Color reconnection and flowlike patterns in pp collisions. Phys. Rev. Lett. **111**, 042001 (2013). http://link.aps.org/doi/10.1103/PhysRevLett.111.042001

12. J. D. Orjuela Koop, A. Adare, D. McGlinchey, and J. L. Nagle, Azimuthal anisotropy relative to the participant plane from a multiphase transport model in central p + Au, d + Au, and ^{3}He + Au collisions at $\sqrt{s_{NN}}$ = 200 gev. Phys. Rev. C **92**, 054903 (2015). https://link.aps.org/doi/10.1103/PhysRevC.92.054903

13. S. Schlichting, P. Tribedy, Collectivity in Small Collision Systems: An Initial-State Perspective. Adv. High Energy Phys. **2016**, 8460349 (2016). arXiv:1611.00329 [hep-ph]

14. B. Schenke, S. Schlichting, P. Tribedy, R. Venugopalan, Mass ordering of spectra from fragmentation of saturated gluon states in high multiplicity proton-proton collisions. Phys. Rev. Lett. **117**(16), 162301 (2016). arXiv:1607.02496 [hep-ph]

15. ALICE Collaboration, B. Abelev et al., Multiplicity dependence of two-particle azimuthal correlations in pp collisions at the LHC. JHEP **09**, 049 (2013). arXiv:1307.1249 [nucl-ex]

16. A. Ortiz, G. Bencedi, H. Bello, Revealing the source of the radial flow patterns in proton-proton collisions using hard probes. J. Phys. G **44**(6), 065001 (2017). arXiv:1608.04784 [hep-ph]

17. ALICE Collaboration, J. Adam et al., Centrality dependence of particle production in p-Pb collisions at $\sqrt{s_{NN}}$= 5.02 TeV. Phys. Rev. C **91**(6), 064905 (2015). arXiv:1412.6828 [nucl-ex]

18. F. Arleo, S.J. Brodsky, D.S. Hwang, A.M. Sickles, Higher-twist dynamics in large transverse momentum hadron production. Phys. Rev. Lett. **105**, 062002 (2010). arXiv:0911.4604 [hep-ph]

19. A. Ortiz, G. Paić, E. Cuautle, Mid-rapidity charged hadron transverse spherocity in pp collisions simulated with Pythia. Nucl. Phys. A **941**, 78–86 (2015). arXiv:1503.03129 [hep-ph]

20. A. Ortiz, Experimental results on event shapes at hadron colliders. Adv. Ser. Direct. High Energy Phys. **29**, 343–357 (2018). arXiv:1705.02056 [hep-ex]

21. ALICE Collaboration, B. Abelev et al., Multiplicity dependence of the average transverse momentum in pp, p-Pb, and Pb-Pb collisions at the LHC. Phys. Lett. B **727**, 371–380 (2013). arXiv:1307.1094 [nucl-ex]

22. ALICE Collaboration, B. Abelev et al., Performance of the ALICE Experiment at the CERN LHC. Int. J. Mod. Phys. A **29**, 1430044 (2014). arXiv:1402.4476 [nucl-ex]

23. T. Sjöstrand, S. Mrenna, P.Z. Skands, PYTHIA 6.4 physics and manual. JHEP **05**, 026 (2006). arXiv:hep-ph/0603175 [hep-ph]

24. P.Z. Skands, Tuning Monte Carlo Generators: The Perugia Tunes. Phys. Rev. D **82**, 074018 (2010). arXiv:1005.3457 [hep-ph]

25. R. Brun, F. Bruyant, F. Carminati, S. Giani, M. Maire, A. McPherson, G. Patrick, L. Urban, GEANT detector description and simulation tool

26. ALICE Collaboration Collaboration, The ALICE definition of primary particles. https://cds.cern.ch/record/2270008

27. ALICE Collaboration, B. Abelev et al., Energy Dependence of the Transverse Momentum Distributions of Charged Particles in pp Collisions Measured by ALICE. Eur. Phys. J. C **73**(12), 2662 (2013). arXiv:1307.1093 [nucl-ex]

28. ALICE Collaboration, J. Adam et al., Pseudorapidity and transverse-momentum distributions of charged particles in proton-proton collisions at $\sqrt{s} = 13$ TeV. Phys. Lett. B **753**, 319–329 (2016). arXiv:1509.08734 [nucl-ex]

29. ALICE Collaboration, S. Acharya et al., Transverse momentum spectra and nuclear modification factors of charged particles in pp, p-Pb and Pb-Pb collisions at the LHC. JHEP **1811**, 013 (2018). https://doi.org/10.1007/JHEP11(2018)013

30. ALICE Collaboration, B. Abelev et al., Centrality Dependence of Charged Particle Production at Large Transverse Momentum in Pb–Pb Collisions at $\sqrt{s_{NN}} = 2.76$ TeV. Phys. Lett. B **720**, 52–62 (2013). arXiv:1208.2711 [hep-ex]

31. R. Hagedorn, Riv. Nuovo Cim **6**, 1 (1983)

32. ALICE Collaboration, B. Abelev et al., Transverse sphericity of primary charged particles in minimum bias proton-proton collisions at $\sqrt{s} = 0.9$, 2.76 and 7 TeV. Eur. Phys. J. C **72**, 2124 (2012). arXiv:1205.3963 [hep-ex]

33. A. Banfi, G.P. Salam, G. Zanderighi, Phenomenology of event shapes at hadron colliders. JHEP **06**, 038 (2010)

34. A. Ortiz, L Valencia Palomo, Universality of the underlying event in pp collisions. Phys. Rev. D **96**(11), 114019 (2017). arXiv:1710.04741 [hep-ex]

35. R.E. Kalman, A new approach to linear filtering and prediction problems. Trans. ASME-J. Basic Eng. 82(Series D), 35–45 (1960)

36. ALICE Collaboration, K. Aamodt et al., Transverse momentum spectra of charged particles in proton-proton collisions at $\sqrt{s} = 900$ GeV with ALICE at the LHC. Phys. Lett. B **693**, 53–68 (2010). arXiv:1007.0719 [hep-ex]

37. T. Pierog, I. Karpenko, J.M. Katzy, E. Yatsenko, K. Werner, EPOS LHC: Test of collective hadronization with data measured at the CERN Large Hadron Collider. Phys. Rev. C **92**(3), 034906 (2015). arXiv:1306.0121 [hep-ph]

38. P. Skands, S. Carrazza, J. Rojo, Tuning PYTHIA 8.1: the Monash 2013 Tune. Eur. Phys. J. C **74**(8), 3024 (2014). arXiv:1404.5630 [hep-ph]

39. ALICE Collaboration, B. Abelev et al., Centrality dependence of π, K, p production in Pb-Pb collisions at $\sqrt{s_{NN}} = 2.76$ TeV. Phys. Rev. C **88**, 044910 (2013). arXiv:1303.0737 [hep-ex]

40. ALICE Collaboration, B. Abelev et al., Neutral pion and η meson production in proton-proton collisions at $\sqrt{s} = 0.9$ TeV and $\sqrt{s} = 7$ TeV. Phys. Lett. B **717**, 162–172 (2012). arXiv:1205.5724 [hep-ex]

41. A.N. Mishra, A. Ortiz, G. Paic, Intriguing similarities of high-p_T particle production between pp and $A - A$ collisions. Phys. Rev. C **99**(3), 034911 (2019). arXiv:1805.04572 [hep-ph]

42. ALICE Collaboration, J. Adam et al., Measurement of charm and beauty production at central rapidity versus charged-particle multiplicity in proton-proton collisions at $\sqrt{s} = 7$ TeV. JHEP **09**, 148 (2015). arXiv:1505.00664 [nucl-ex]

43. T. Sjöstrand, M. van Zijl, A Multiple Interaction Model for the Event Structure in Hadron Collisions. Phys. Rev. D **36**, 2019 (1987)

44. C.M.S. Collaboration, S. Chatrchyan et al., Jet and underlying event properties as a function of charged-particle multiplicity in proton-proton collisions at $\sqrt{s} = 7$ TeV. Eur. Phys. J. C **73**(12), 2674 (2013). arXiv:1310.4554 [hep-ex]

45. ATLAS Collaboration, G. Aad et al., Measurement of charged-particle event shape variables in $\sqrt{s} = 7$ TeV proton-proton interactions with the ATLAS detector. Phys. Rev. D **88**(3), 032004 (2013). arXiv:1207.6915 [hep-ex]

ALICE Collaboration

S. Acharya[141], D. Adamová[93], S. P. Adhya[141], A. Adler[74], J. Adolfsson[80], M. M. Aggarwal[98], G. Aglieri Rinella[34], M. Agnello[31], N. Agrawal[10], Z. Ahammed[141], S. Ahmad[17], S. U. Ahn[76], S. Aiola[146], A. Akindinov[64], M. Al-Turany[105], S. N. Alam[141], D. S. D. Albuquerque[122], D. Aleksandrov[87], B. Alessandro[58], H. M. Alfanda[6], R. Alfaro Molina[72], B. Ali[17], Y. Ali[15], A. Alici[10,27,53], A. Alkin[2], J. Alme[22], T. Alt[69], L. Altenkamper[22], I. Altsybeev[112], M. N. Anaam[6], C. Andrei[47], D. Andreou[34], H. A. Andrews[109], A. Andronic[144], M. Angeletti[34], V. Anguelov[102], C. Anson[16], T. Antičić[106], F. Antinori[56], P. Antonioli[53], R. Anwar[126], N. Apadula[79], L. Aphecetche[114], H. Appelshäuser[69], S. Arcelli[27], R. Arnaldi[58], M. Arratia[79], I. C. Arsene[21], M. Arslandok[102], A. Augustinus[34], R. Averbeck[105], S. Aziz[61], M. D. Azmi[17], A. Badalà[55], Y. W. Baek[40], S. Bagnasco[58], X. Bai[105], R. Bailhache[69], R. Bala[99], A. Baldisseri[137], M. Ball[42], R. C. Baral[85], R. Barbera[28], L. Barioglio[26], G. G. Barnaföldi[145], L. S. Barnby[92], V. Barret[134], P. Bartalini[6], K. Barth[34], E. Bartsch[69], F. Baruffaldi[29], N. Bastid[134], S. Basu[143], G. Batigne[114], B. Batyunya[75], P. C. Batzing[21], D. Bauri[48], J. L. Bazo Alba[110], I. G. Bearden[88], C. Bedda[63], N. K. Behera[60], I. Belikov[136], F. Bellini[34], R. Bellwied[126], V. Belyaev[91], G. Bencedi[145], S. Beole[26], A. Bercuci[47], Y. Berdnikov[96], D. Berenyi[145], R. A. Bertens[130], D. Berzano[58], M. G. Besoiu[68], L. Betev[34], A. Bhasin[99], I. R. Bhat[99], H. Bhatt[48], B. Bhattacharjee[41], A. Bianchi[26], L. Bianchi[26,126],

N. Bianchi[51], J. Bielčík[37], J. Bielčíková[93], A. Bilandzic[103,117], G. Biro[145], R. Biswas[3], S. Biswas[3], J. T. Blair[119], D. Blau[87], C. Blume[69], G. Boca[139], F. Bock[34,94], A. Bogdanov[91], L. Boldizsár[145], A. Bolozdynya[91], M. Bombara[38], G. Bonomi[140], H. Borel[137], A. Borissov[91,144], M. Borri[128], H. Bossi[146], E. Botta[26], C. Bourjau[88], L. Bratrud[69], P. Braun-Munzinger[105], M. Bregant[121], T. A. Broker[69], M. Broz[37], E. J. Brucken[43], E. Bruna[58], G. E. Bruno[33,104], M. D. Buckland[128], D. Budnikov[107], H. Buesching[69], S. Bufalino[31], O. Bugnon[114], P. Buhler[113], P. Buncic[34], Z. Buthelezi[73], J. B. Butt[15], J. T. Buxton[95], D. Caffarri[89], A. Caliva[105], E. Calvo Villar[110], R. S. Camacho[44], P. Camerini[25], A. A. Capon[113], F. Carnesecchi[10], J. Castillo Castellanos[137], A. J. Castro[130], E. A. R. Casula[54], F. Catalano[31], C. Ceballos Sanchez[52], P. Chakraborty[48], S. Chandra[141], B. Chang[127], W. Chang[6], S. Chapeland[34], M. Chartier[128], S. Chattopadhyay[141], S. Chattopadhyay[108], A. Chauvin[24], C. Cheshkov[135], B. Cheynis[135], V. Chibante Barroso[34], D. D. Chinellato[122], S. Cho[60], P. Chochula[34], T. Chowdhury[134], P. Christakoglou[89], C. H. Christensen[88], P. Christiansen[80], T. Chujo[133], C. Cicalo[54], L. Cifarelli[10,27], F. Cindolo[53], J. Cleymans[125], F. Colamaria[52], D. Colella[52], A. Collu[79], M. Colocci[27], M. Concas[58,b], G. Conesa Balbastre[78], Z. Conesa del Valle[61], G. Contin[59,128], J. G. Contreras[37], T. M. Cormier[94], Y. Corrales Morales[26,58], P. Cortese[32], M. R. Cosentino[123], F. Costa[34], S. Costanza[139], J. Crkovská[61], P. Crochet[134], E. Cuautle[70], L. Cunqueiro[94], D. Dabrowski[142], T. Dahms[103,117], A. Dainese[56], F. P. A. Damas[114,137], S. Dani[66], M. C. Danisch[102], A. Danu[68], D. Das[108], I. Das[108], S. Das[3], A. Dash[85], S. Dash[48], A. Dashi[103], S. De[49,85], A. De Caro[30], G. de Cataldo[52], C. de Conti[121], J. de Cuveland[39], A. De Falco[24], D. De Gruttola[10], N. De Marco[58], S. De Pasquale[30], R. D. De Souza[122], S. Deb[49], H. F. Degenhardt[121], K. R. Deja[142], A. Deloff[84], S. Delsanto[26,131], P. Dhankher[48], D. Di Bari[33], A. Di Mauro[34], R. A. Diaz[8], T. Dietel[125], P. Dillenseger[69], Y. Ding[6], R. Divià[34], Ø. Djuvsland[22], U. Dmitrieva[62], A. Dobrin[34,68], B. Dönigus[69], O. Dordic[21], A. K. Dubey[141], A. Dubla[105], S. Dudi[98], M. Dukhishyam[85], P. Dupieux[134], R. J. Ehlers[146], D. Elia[52], H. Engel[74], E. Epple[146], B. Erazmus[114], F. Erhardt[97], A. Erokhin[112], M. R. Ersdal[22], B. Espagnon[61], G. Eulisse[34], J. Eum[18], D. Evans[109], S. Evdokimov[90], L. Fabbietti[103,117], M. Faggin[29], J. Faivre[78], A. Fantoni[51], M. Fasel[94], P. Fecchio[31], L. Feldkamp[144], A. Feliciello[58], G. Feofilov[112], A. Fernández Téllez[44], A. Ferrero[137], A. Ferretti[26], A. Festanti[34], V. J. G. Feuillard[102], J. Figiel[118], S. Filchagin[107], D. Finogeev[62], F. M. Fionda[22], G. Fiorenza[52], F. Flor[126], S. Foertsch[73], P. Foka[105], S. Fokin[87], E. Fragiacomo[59], U. Frankenfeld[105], G. G. Fronze[26], U. Fuchs[34], C. Furget[78], A. Furs[62], M. Fusco Girard[30], J. J. Gaardhøje[88], M. Gagliardi[26], A. M. Gago[110], A. Gal[136], C. D. Galvan[120], P. Ganoti[83], C. Garabatos[105], E. Garcia-Solis[11], K. Garg[28], C. Gargiulo[34], K. Garner[144], P. Gasik[103,117], E. F. Gauger[119], M. B. Gay Ducati[71], M. Germain[114], J. Ghosh[108], P. Ghosh[141], S. K. Ghosh[3], P. Gianotti[51], P. Giubellino[58,105], P. Giubilato[29], P. Glässel[102], D. M. Goméz Coral[72], A. Gomez Ramirez[74], V. Gonzalez[105], P. González-Zamora[44], S. Gorbunov[39], L. Görlich[118], S. Gotovac[35], V. Grabski[72], L. K. Graczykowski[142], K. L. Graham[109], L. Greiner[79], A. Grelli[63], C. Grigoras[34], V. Grigoriev[91], A. Grigoryan[1], S. Grigoryan[75], O. S. Groettvik[22], J. M. Gronefeld[105], F. Grosa[31], J. F. Grosse-Oetringhaus[34], R. Grosso[105], R. Guernane[78], B. Guerzoni[27], M. Guittiere[114], K. Gulbrandsen[88], T. Gunji[132], A. Gupta[99], R. Gupta[99], I. B. Guzman[44], R. Haake[34,146], M. K. Habib[105], C. Hadjidakis[61], H. Hamagaki[81], G. Hamar[145], M. Hamid[6], R. Hannigan[119], M. R. Haque[63], A. Harlenderova[105], J. W. Harris[146], A. Harton[11], J. A. Hasenbichler[34], H. Hassan[78], D. Hatzifotiadou[10,53], P. Hauer[42], S. Hayashi[132], S. T. Heckel[69], E. Hellbär[69], H. Helstrup[36], A. Herghelegiu[47], E. G. Hernandez[44], G. Herrera Corral[9], F. Herrmann[144], K. F. Hetland[36], T. E. Hilden[43], H. Hillemanns[34], C. Hills[128], B. Hippolyte[136], B. Hohlweger[103], D. Horak[37], S. Hornung[105], R. Hosokawa[133], P. Hristov[34], C. Huang[61], C. Hughes[130], P. Huhn[69], T. J. Humanic[95], H. Hushnud[108], L. A. Husova[144], N. Hussain[41], S. A. Hussain[15], T. Hussain[17], D. Hutter[39], D. S. Hwang[19], J. P. Iddon[34,128], R. Ilkaev[107], M. Inaba[133], M. Ippolitov[87], M. S. Islam[108], M. Ivanov[105], V. Ivanov[96], V. Izucheev[90], B. Jacak[79], N. Jacazio[27], P. M. Jacobs[79], M. B. Jadhav[48], S. Jadlovska[116], J. Jadlovsky[116], S. Jaelani[63], C. Jahnke[121], M. J. Jakubowska[142], M. A. Janik[142], M. Jercic[97], O. Jevons[109], R. T. Jimenez Bustamante[105], M. Jin[126], F. Jonas[94,144], P. G. Jones[109], A. Jusko[109], P. Kalinak[65], A. Kalweit[34], J. H. Kang[147], V. Kaplin[91], S. Kar[6], A. Karasu Uysal[77], O. Karavichev[62], T. Karavicheva[62], P. Karczmarczyk[34], E. Karpechev[62], U. Kebschull[74], R. Keidel[46], M. Keil[34], B. Ketzer[42], Z. Khabanova[89], A. M. Khan[6], S. Khan[17], S. A. Khan[141], A. Khanzadeev[96], Y. Kharlov[90], A. Khatun[17], A. Khuntia[49,118], B. Kileng[36], B. Kim[60], B. Kim[133], D. Kim[147], D. J. Kim[127], E. J. Kim[13], H. Kim[147], J. Kim[147], J. S. Kim[40], J. Kim[102], J. Kim[147], J. Kim[13], M. Kim[102], S. Kim[19], T. Kim[147], T. Kim[147], S. Kirsch[39], I. Kisel[39], S. Kiselev[64], A. Kisiel[142], J. L. Klay[5], C. Klein[69], J. Klein[58], S. Klein[79], C. Klein-Bösing[144], S. Klewin[102], A. Kluge[34], M. L. Knichel[34], A. G. Knospe[126], C. Kobdaj[115], M. K. Köhler[102], T. Kollegger[105], A. Kondratyev[75], N. Kondratyeva[91], E. Kondratyuk[90], P. J. Konopka[34], L. Koska[116], O. Kovalenko[84], V. Kovalenko[112], M. Kowalski[118], I. Králik[65], A. Kravčáková[38], L. Kreis[105], M. Krivda[65,109], F. Krizek[93], K. Krizkova Gajdosova[37], M. Krüger[69], E. Kryshen[96], M. Krzewicki[39], A. M. Kubera[95], V. Kučera[60], C. Kuhn[136], P. G. Kuijer[89], L. Kumar[98], S. Kumar[48], S. Kundu[85], P. Kurashvili[84], A. Kurepin[62], A. B. Kurepin[62], S. Kushpil[93], J. Kvapil[109], M. J. Kweon[60], J. Y. Kwon[60], Y. Kwon[147], S. L. La Pointe[39], P. La Rocca[28], Y. S. Lai[79], R. Langoy[124], K. Lapidus[34,146], A. Lardeux[21], P. Larionov[51], E. Laudi[34], R. Lavicka[37], T. Lazareva[112], R. Lea[25],

L. Leardini[102], S. Lee[147], F. Lehas[89], S. Lehner[113], J. Lehrbach[39], R. C. Lemmon[92], I. León Monzón[120], E. D. Lesser[20], M. Lettrich[34], P. Lévai[145], X. Li[12], X. L. Li[6], J. Lien[124], R. Lietava[109], B. Lim[18], S. Lindal[21], V. Lindenstruth[39], S. W. Lindsay[128], C. Lippmann[105], M. A. Lisa[95], V. Litichevskyi[43], A. Liu[79], S. Liu[95], W. J. Llope[143], I. M. Lofnes[22], V. Loginov[91], C. Loizides[94], P. Loncar[35], X. Lopez[134], E. López Torres[8], P. Luettig[69], J. R. Luhder[144], M. Lunardon[29], G. Luparello[59], M. Lupi[74], A. Maevskaya[62], M. Mager[34], S. M. Mahmood[21], T. Mahmoud[42], A. Maire[136], R. D. Majka[146], M. Malaev[96], Q. W. Malik[21], L. Malinina[75,c], D. Mal'Kevich[64], P. Malzacher[105], A. Mamonov[107], V. Manko[87], F. Manso[134], V. Manzari[52], Y. Mao[6], M. Marchisone[135], J. Mareš[67], G. V. Margagliotti[25], A. Margotti[53], J. Margutti[63], A. Marín[105], C. Markert[119], M. Marquard[69], N. A. Martin[102], P. Martinengo[34], J. L. Martinez[126], M. I. Martínez[44], G. Martínez García[114], M. Martinez Pedreira[34], S. Masciocchi[105], M. Masera[26], A. Masoni[54], L. Massacrier[61], E. Masson[114], A. Mastroserio[52,138], A. M. Mathis[103,117], P. F. T. Matuoka[121], A. Matyja[118], C. Mayer[118], M. Mazzilli[33], M. A. Mazzoni[57], A. F. Mechler[69], F. Meddi[23], Y. Melikyan[91], A. Menchaca-Rocha[72], E. Meninno[30], M. Meres[14], S. Mhlanga[125], Y. Miake[133], L. Micheletti[26], M. M. Mieskolainen[43], D. L. Mihaylov[103], K. Mikhaylov[64,75], A. Mischke[63], A. N. Mishra[70], D. Miśkowiec[105], C. M. Mitu[68], N. Mohammadi[34], A. P. Mohanty[63], B. Mohanty[85], M. Mohisin Khan[17,d], M. Mondal[141], M. M. Mondal[66], C. Mordasini[103], D. A. Moreira De Godoy[144], L. A. P. Moreno[44], S. Moretto[29], A. Morreale[114], A. Morsch[34], T. Mrnjavac[34], V. Muccifora[51], E. Mudnic[35], D. Mühlheim[144], S. Muhuri[141], J. D. Mulligan[79,146], M. G. Munhoz[121], K. Münning[42], R. H. Munzer[69], H. Murakami[132], S. Murray[73], L. Musa[34], J. Musinsky[65], C. J. Myers[126], J. W. Myrcha[142], B. Naik[48], R. Nair[84], B. K. Nandi[48], R. Nania[10,53], E. Nappi[52], M. U. Naru[15], A. F. Nassirpour[80], H. Natal da Luz[121], C. Nattrass[130], R. Nayak[48], T. K. Nayak[85,141], S. Nazarenko[107], R. A. Negrao De Oliveira[69], L. Nellen[70], S. V. Nesbo[36], G. Neskovic[39], B. S. Nielsen[88], S. Nikolaev[87], S. Nikulin[87], V. Nikulin[96], F. Noferini[10,53], P. Nomokonov[75], G. Nooren[63], J. Norman[78], P. Nowakowski[142], A. Nyanin[87], J. Nystrand[22], M. Ogino[81], A. Ohlson[102], J. Oleniacz[142], A. C. Oliveira Da Silva[121], M. H. Oliver[146], C. Oppedisano[58], R. Orava[43], A. Ortiz Velasquez[70], A. Oskarsson[80], J. Otwinowski[118], K. Oyama[81], Y. Pachmayer[102], V. Pacik[88], D. Pagano[140], G. Paić[70], P. Palni[6], J. Pan[143], A. K. Pandey[48], S. Panebianco[137], V. Papikyan[1], P. Pareek[49], J. Park[60], J. E. Parkkila[127], S. Parmar[98], A. Passfeld[144], S. P. Pathak[126], R. N. Patra[141], B. Paul[24,58], H. Pei[6], T. Peitzmann[63], X. Peng[6], L. G. Pereira[71], H. Pereira Da Costa[137], D. Peresunko[87], G. M. Perez[8], E. Perez Lezama[69], V. Peskov[69], Y. Pestov[4], V. Petráček[37], M. Petrovici[47], R. P. Pezzi[71], S. Piano[59], M. Pikna[14], P. Pillot[114], L. O. D. L. Pimentel[88], O. Pinazza[34,53], L. Pinsky[126], S. Pisano[51], D. B. Piyarathna[126], M. Płoskoń[79], M. Planinic[97], F. Pliquett[69], J. Pluta[142], S. Pochybova[145], M. G. Poghosyan[94], B. Polichtchouk[90], N. Poljak[97], W. Poonsawat[115], A. Pop[47], H. Poppenborg[144], S. Porteboeuf-Houssais[134], V. Pozdniakov[75], S. K. Prasad[3], R. Preghenella[53], F. Prino[58], C. A. Pruneau[143], I. Pshenichnov[62], M. Puccio[26,34], V. Punin[107], K. Puranapanda[141], J. Putschke[143], R. E. Quishpe[126], S. Ragoni[109], S. Raha[3], S. Rajput[99], J. Rak[127], A. Rakotozafindrabe[137], L. Ramello[32], F. Rami[136], R. Raniwala[100], S. Raniwala[100], S. S. Räsänen[43], B. T. Rascanu[69], R. Rath[49], V. Ratza[42], I. Ravasenga[31], K. F. Read[94,130], K. Redlich[84,e], A. Rehman[22], P. Reichelt[69], F. Reidt[34], X. Ren[6], R. Renfordt[69], A. Reshetin[62], J.-P. Revol[10], K. Reygers[102], V. Riabov[96], T. Richert[80,88], M. Richter[21], P. Riedler[34], W. Riegler[34], F. Riggi[28], C. Ristea[68], S. P. Rode[49], M. Rodríguez Cahuantzi[44], K. Røed[21], R. Rogalev[90], E. Rogochaya[75], D. Rohr[34], D. Röhrich[22], P. S. Rokita[142], F. Ronchetti[51], E. D. Rosas[70], K. Roslon[142], P. Rosnet[134], A. Rossi[29], A. Rotondi[139], F. Roukoutakis[83], A. Roy[49], P. Roy[108], O. V. Rueda[80], R. Rui[25], B. Rumyantsev[75], A. Rustamov[86], E. Ryabinkin[87], Y. Ryabov[96], A. Rybicki[118], H. Rytkonen[127], S. Saarinen[43], S. Sadhu[141], S. Sadovsky[90], K. Šafařík[34,37], S. K. Saha[141], B. Sahoo[48], P. Sahoo[49], R. Sahoo[49], S. Sahoo[66], P. K. Sahu[66], J. Saini[141], S. Sakai[133], S. Sambyal[99], V. Samsonov[91,96], A. Sandoval[72], A. Sarkar[73], D. Sarkar[141,143], N. Sarkar[141], P. Sarma[41], V. M. Sarti[103], M. H. P. Sas[63], E. Scapparone[53], B. Schaefer[94], J. Schambach[119], H. S. Scheid[69], C. Schiaua[47], R. Schicker[102], A. Schmah[102], C. Schmidt[105], H. R. Schmidt[101], M. O. Schmidt[102], M. Schmidt[101], N. V. Schmidt[69,94], A. R. Schmier[130], J. Schukraft[34,88], Y. Schutz[34,136], K. Schwarz[105], K. Schweda[105], G. Scioli[27], E. Scomparin[58], M. Šefčík[38], J. E. Seger[16], Y. Sekiguchi[132], D. Sekihata[45], I. Selyuzhenkov[91,105], S. Senyukov[136], D. Serebryakov[62], E. Serradilla[72], P. Sett[48], A. Sevcenco[68], A. Shabanov[62], A. Shabetai[114], R. Shahoyan[34], W. Shaikh[108], A. Shangaraev[90], A. Sharma[98], A. Sharma[99], M. Sharma[99], N. Sharma[98], A. I. Sheikh[141], K. Shigaki[45], M. Shimomura[82], S. Shirinkin[64], Q. Shou[111], Y. Sibiriak[87], S. Siddhanta[54], T. Siemiarczuk[84], D. Silvermyr[80], C. Silvestre[78], G. Simatovic[89], G. Simonetti[34,103], R. Singh[85], R. Singh[99], V. K. Singh[141], V. Singhal[141], T. Sinha[108], B. Sitar[14], M. Sitta[32], T. B. Skaali[21], M. Slupecki[127], N. Smirnov[146], R. J. M. Snellings[63], T. W. Snellman[127], J. Sochan[116], C. Soncco[110], J. Song[60,126], A. Songmoolnak[115], F. Soramel[29], S. Sorensen[130], I. Sputowska[118], J. Stachel[102], I. Stan[68], P. Stankus[94], P. J. Steffanic[130], E. Stenlund[80], D. Stocco[114], M. M. Storetvedt[36], P. Strmen[14], A. A. P. Suaide[121], T. Sugitate[45], C. Suire[61], M. Suleymanov[15], M. Suljic[34], R. Sultanov[64], M. Šumbera[93], S. Sumowidagdo[50], K. Suzuki[113], S. Swain[66], A. Szabo[14], I. Szarka[14], U. Tabassam[15], G. Taillepied[134], J. Takahashi[122], G. J. Tambave[22], S. Tang[6,134], M. Tarhini[114], M. G. Tarzila[47], A. Tauro[34], G. Tejeda Muñoz[44], A. Telesca[34], C. Terrevoli[29,126], D. Thakur[49], S. Thakur[141], D. Thomas[119], F. Thoresen[88], R. Tieulent[135], A. Tikhonov[62],

A. R. Timmins[126], A. Toia[69], N. Topilskaya[62], M. Toppi[51], F. Torales-Acosta[20], S. R. Torres[120], S. Tripathy[49], T. Tripathy[48], S. Trogolo[26,29], G. Trombetta[33], L. Tropp[38], V. Trubnikov[2], W. H. Trzaska[127], T. P. Trzcinski[142], B. A. Trzeciak[63], T. Tsuji[132], A. Tumkin[107], R. Turrisi[56], T. S. Tveter[21], K. Ullaland[22], E. N. Umaka[126], A. Uras[135], G. L. Usai[24], A. Utrobicic[97], M. Vala[38,116], N. Valle[139], S. Vallero[58], N. van der Kolk[63], L. V. R. van Doremalen[63], M. van Leeuwen[63], P. Vande Vyvre[34], D. Varga[145], M. Varga-Kofarago[145], A. Vargas[44], M. Vargyas[127], R. Varma[48], M. Vasileiou[83], A. Vasiliev[87], O. Vázquez Doce[103,117], V. Vechernin[112], A. M. Veen[63], E. Vercellin[26], S. Vergara Limón[44], L. Vermunt[63], R. Vernet[7], R. Vértesi[145], L. Vickovic[35], J. Viinikainen[127], Z. Vilakazi[131], O. Villalobos Baillie[109], A. Villatoro Tello[44], G. Vino[52], A. Vinogradov[87], T. Virgili[30], V. Vislavicius[88], A. Vodopyanov[75], B. Volkel[34], M. A. Völkl[101], K. Voloshin[64], S. A. Voloshin[143], G. Volpe[33], B. von Haller[34], I. Vorobyev[103,117], D. Voscek[116], J. Vrláková[38], B. Wagner[22], Y. Watanabe[133], M. Weber[113], S. G. Weber[105], A. Wegrzynek[34], D. F. Weiser[102], S. C. Wenzel[34], J. P. Wessels[144], E. Widmann[113], J. Wiechula[69], J. Wikne[21], G. Wilk[84], J. Wilkinson[53], G. A. Willems[34], E. Willsher[109], B. Windelband[102], W. E. Witt[130], Y. Wu[129], R. Xu[6], S. Yalcin[77], K. Yamakawa[45], S. Yang[22], S. Yano[137], Z. Yin[6], H. Yokoyama[63], I.-K. Yoo[18], J. H. Yoon[60], S. Yuan[22], A. Yuncu[102], V. Yurchenko[2], V. Zaccolo[25,58], A. Zaman[15], C. Zampolli[34], H. J. C. Zanoli[121], N. Zardoshti[34], A. Zarochentsev[112], P. Závada[67], N. Zaviyalov[107], H. Zbroszczyk[142], M. Zhalov[96], X. Zhang[6], Z. Zhang[6,134], C. Zhao[21], V. Zherebchevskii[112], N. Zhigareva[64], D. Zhou[6], Y. Zhou[88], Z. Zhou[22], J. Zhu[6], Y. Zhu[6], A. Zichichi[10,27], M. B. Zimmermann[34], G. Zinovjev[2], N. Zurlo[140]

1 A.I. Alikhanyan National Science Laboratory (Yerevan Physics Institute) Foundation, Yerevan, Armenia

2 Bogolyubov Institute for Theoretical Physics, National Academy of Sciences of Ukraine, Kiev, Ukraine

3 Bose Institute, Department of Physics and Centre for Astroparticle Physics and Space Science (CAPSS), Kolkata, India

4 Budker Institute for Nuclear Physics, Novosibirsk, Russia

5 California Polytechnic State University, San Luis Obispo, CA, USA

6 Central China Normal University, Wuhan, China

7 Centre de Calcul de l'IN2P3, Villeurbanne, Lyon, France

8 Centro de Aplicaciones Tecnológicas y Desarrollo Nuclear (CEADEN), Havana, Cuba

9 Centro de Investigación y de Estudios Avanzados (CINVESTAV), Mexico City and Mérida, Mexico

10 Centro Fermi - Museo Storico della Fisica e Centro Studi e Ricerche "Enrico Fermi", Rome, Italy

11 Chicago State University, Chicago, IL, USA

12 China Institute of Atomic Energy, Beijing, China

13 Chonbuk National University, Jeonju, Republic of Korea

14 Comenius University Bratislava, Faculty of Mathematics, Physics and Informatics, Bratislava, Slovakia

15 COMSATS University Islamabad, Islamabad, Pakistan

16 Creighton University, Omaha, NE, USA

17 Department of Physics, Aligarh Muslim University, Aligarh, India

18 Department of Physics, Pusan National University, Pusan, Republic of Korea

19 Department of Physics, Sejong University, Seoul, Republic of Korea

20 Department of Physics, University of California, Berkeley, CA, USA

21 Department of Physics, University of Oslo, Oslo, Norway

22 Department of Physics and Technology, University of Bergen, Bergen, Norway

23 Dipartimento di Fisica dell'Università 'La Sapienza' and Sezione INFN, Rome, Italy

24 Dipartimento di Fisica dell'Università and Sezione INFN, Cagliari, Italy

25 Dipartimento di Fisica dell'Università and Sezione INFN, Trieste, Italy

26 Dipartimento di Fisica dell'Università and Sezione INFN, Turin, Italy

27 Dipartimento di Fisica e Astronomia dell'Università and Sezione INFN, Bologna, Italy

28 Dipartimento di Fisica e Astronomia dell'Università and Sezione INFN, Catania, Italy

29 Dipartimento di Fisica e Astronomia dell'Università and Sezione INFN, Padova, Italy

30 Dipartimento di Fisica 'E.R. Caianiello' dell'Università and Gruppo Collegato INFN, Salerno, Italy

31 Dipartimento DISAT del Politecnico and Sezione INFN, Turin, Italy

32 Dipartimento di Scienze e Innovazione Tecnologica dell'Università del Piemonte Orientale and INFN Sezione di Torino, Alessandria, Italy

33 Dipartimento Interateneo di Fisica 'M. Merlin' and Sezione INFN, Bari, Italy

34 European Organization for Nuclear Research (CERN), Geneva, Switzerland

35 Faculty of Electrical Engineering, Mechanical Engineering and Naval Architecture, University of Split, Split, Croatia

[36] Faculty of Engineering and Science, Western Norway University of Applied Sciences, Bergen, Norway

[37] Faculty of Nuclear Sciences and Physical Engineering, Czech Technical University in Prague, Prague, Czech Republic

[38] Faculty of Science, P.J. Šafárik University, Košice, Slovakia

[39] Frankfurt Institute for Advanced Studies, Johann Wolfgang Goethe-Universität Frankfurt, Frankfurt, Germany

[40] Gangneung-Wonju National University, Gangneung, Republic of Korea

[41] Gauhati University, Department of Physics, Guwahati, India

[42] Helmholtz-Institut für Strahlen- und Kernphysik, Rheinische Friedrich-Wilhelms-Universität Bonn, Bonn, Germany

[43] Helsinki Institute of Physics (HIP), Helsinki, Finland

[44] High Energy Physics Group, Universidad Autónoma de Puebla, Puebla, Mexico

[45] Hiroshima University, Hiroshima, Japan

[46] Hochschule Worms, Zentrum für Technologietransfer und Telekommunikation (ZTT), Worms, Germany

[47] Horia Hulubei National Institute of Physics and Nuclear Engineering, Bucharest, Romania

[48] Indian Institute of Technology Bombay (IIT), Mumbai, India

[49] Indian Institute of Technology Indore, Indore, India

[50] Indonesian Institute of Sciences, Jakarta, Indonesia

[51] INFN, Laboratori Nazionali di Frascati, Frascati, Italy

[52] INFN, Sezione di Bari, Bari, Italy

[53] INFN, Sezione di Bologna, Bologna, Italy

[54] INFN, Sezione di Cagliari, Cagliari, Italy

[55] INFN, Sezione di Catania, Catania, Italy

[56] INFN, Sezione di Padova, Padova, Italy

[57] INFN, Sezione di Roma, Rome, Italy

[58] INFN, Sezione di Torino, Turin, Italy

[59] INFN, Sezione di Trieste, Trieste, Italy

[60] Inha University, Incheon, Republic of Korea

[61] Institut de Physique Nucléaire d'Orsay (IPNO), Institut National de Physique Nucléaire et de Physique des Particules (IN2P3/CNRS), Université de Paris-Sud, Université Paris-Saclay, Orsay, France

[62] Institute for Nuclear Research, Academy of Sciences, Moscow, Russia

[63] Institute for Subatomic Physics, Utrecht University/Nikhef, Utrecht, Netherlands

[64] Institute for Theoretical and Experimental Physics, Moscow, Russia

[65] Institute of Experimental Physics, Slovak Academy of Sciences, Košice, Slovakia

[66] Institute of Physics, Homi Bhabha National Institute, Bhubaneswar, India

[67] Institute of Physics of the Czech Academy of Sciences, Prague, Czech Republic

[68] Institute of Space Science (ISS), Bucharest, Romania

[69] Institut für Kernphysik, Johann Wolfgang Goethe-Universität Frankfurt, Frankfurt, Germany

[70] Instituto de Ciencias Nucleares, Universidad Nacional Autónoma de México, Mexico City, Mexico

[71] Instituto de Física, Universidade Federal do Rio Grande do Sul (UFRGS), Porto Alegre, Brazil

[72] Instituto de Física, Universidad Nacional Autónoma de México, Mexico City, Mexico

[73] iThemba LABS, National Research Foundation, Somerset West, South Africa

[74] Johann-Wolfgang-Goethe Universität Frankfurt Institut für Informatik, Fachbereich Informatik und Mathematik, Frankfurt, Germany

[75] Joint Institute for Nuclear Research (JINR), Dubna, Russia

[76] Korea Institute of Science and Technology Information, Daejeon, Republic of Korea

[77] KTO Karatay University, Konya, Turkey

[78] Laboratoire de Physique Subatomique et de Cosmologie, Université Grenoble-Alpes, CNRS-IN2P3, Grenoble, France

[79] Lawrence Berkeley National Laboratory, Berkeley, CA, USA

[80] Lund University Department of Physics, Division of Particle Physics, Lund, Sweden

[81] Nagasaki Institute of Applied Science, Nagasaki, Japan

[82] Nara Women's University (NWU), Nara, Japan

[83] National and Kapodistrian University of Athens, School of Science, Department of Physics , Athens, Greece

[84] National Centre for Nuclear Research, Warsaw, Poland

[85] National Institute of Science Education and Research, Homi Bhabha National Institute, Jatni, India

[86] National Nuclear Research Center, Baku, Azerbaijan

[87] National Research Centre Kurchatov Institute, Moscow, Russia

[88] Niels Bohr Institute, University of Copenhagen, Copenhagen, Denmark

[89] Nikhef, National institute for subatomic physics, Amsterdam, Netherlands

[90] NRC Kurchatov Institute IHEP, Protvino, Russia

[91] NRNU Moscow Engineering Physics Institute, Moscow, Russia

[92] Nuclear Physics Group, STFC Daresbury Laboratory, Daresbury, UK

[93] Nuclear Physics Institute of the Czech Academy of Sciences, Řež u Prahy, Czech Republic

[94] Oak Ridge National Laboratory, Oak Ridge, TN, USA

[95] Ohio State University, Columbus, OH, USA

[96] Petersburg Nuclear Physics Institute, Gatchina, Russia

[97] Physics department, Faculty of science, University of Zagreb, Zagreb, Croatia

[98] Physics Department, Panjab University, Chandigarh, India

[99] Physics Department, University of Jammu, Jammu, India

[100] Physics Department, University of Rajasthan, Jaipur, India

[101] Physikalisches Institut, Eberhard-Karls-Universität Tübingen, Tübingen, Germany

[102] Physikalisches Institut, Ruprecht-Karls-Universität Heidelberg, Heidelberg, Germany

[103] Physik Department, Technische Universität München, Munich, Germany

[104] Politecnico di Bari, Bari, Italy

[105] Research Division and ExtreMe Matter Institute EMMI, GSI Helmholtzzentrum für Schwerionenforschung GmbH, Darmstadt, Germany

[106] Rudjer Bošković Institute, Zagreb, Croatia

[107] Russian Federal Nuclear Center (VNIIEF), Sarov, Russia

[108] Saha Institute of Nuclear Physics, Homi Bhabha National Institute, Kolkata, India

[109] School of Physics and Astronomy, University of Birmingham, Birmingham, UK

[110] Sección Física, Departamento de Ciencias, Pontificia Universidad Católica del Perú, Lima, Peru

[111] Shanghai Institute of Applied Physics, Shanghai, China

[112] St. Petersburg State University, St. Petersburg, Russia

[113] Stefan Meyer Institut für Subatomare Physik (SMI), Vienna, Austria

[114] SUBATECH, IMT Atlantique, Université de Nantes, CNRS-IN2P3, Nantes, France

[115] Suranaree University of Technology, Nakhon Ratchasima, Thailand

[116] Technical University of Košice, Košice, Slovakia

[117] Technische Universität München, Excellence Cluster 'Universe', Munich, Germany

[118] The Henryk Niewodniczanski Institute of Nuclear Physics, Polish Academy of Sciences, Cracow, Poland

[119] The University of Texas at Austin, Austin, TX, USA

[120] Universidad Autónoma de Sinaloa, Culiacán, Mexico

[121] Universidade de São Paulo (USP), São Paulo, Brazil

[122] Universidade Estadual de Campinas (UNICAMP), Campinas, Brazil

[123] Universidade Federal do ABC, Santo Andre, Brazil

[124] University College of Southeast Norway, Tonsberg, Norway

[125] University of Cape Town, Cape Town, South Africa

[126] University of Houston, Houston, TX, USA

[127] University of Jyväskylä, Jyväskylä, Finland

[128] University of Liverpool, Liverpool, UK

[129] University of Science and Techonology of China, Hefei, China

[130] University of Tennessee, Knoxville, TN, USA

[131] University of the Witwatersrand, Johannesburg, South Africa

[132] University of Tokyo, Tokyo, Japan

[133] University of Tsukuba, Tsukuba, Japan

[134] Université Clermont Auvergne, CNRS/IN2P3, LPC, Clermont-Ferrand, France

[135] Université de Lyon, Université Lyon 1, CNRS/IN2P3, IPN-Lyon, Villeurbanne, Lyon, France

[136] Université de Strasbourg, CNRS, IPHC UMR 7178, F-67000 Strasbourg, France, Strasbourg, France

[137] Université Paris-Saclay Centre d'Etudes de Saclay (CEA), IRFU, Départment de Physique Nucléaire (DPhN), Saclay, France

[138] Università degli Studi di Foggia, Foggia, Italy

[139] Università degli Studi di Pavia, Pavia, Italy

[140] Università di Brescia, Brescia, Italy

[141] Variable Energy Cyclotron Centre, Homi Bhabha National Institute, Kolkata, India

[142] Warsaw University of Technology, Warsaw, Poland

[143] Wayne State University, Detroit, MI, USA

[144] Westfälische Wilhelms-Universität Münster, Institut für Kernphysik, Münster, Germany

[145] Wigner Research Centre for Physics, Hungarian Academy of Sciences, Budapest, Hungary

[146] Yale University, New Haven, CT, USA

[147] Yonsei University, Seoul, Republic of Korea

[a] Deceased

[b] Dipartimento DET del Politecnico di Torino, Turin, Italy

[c] M.V. Lomonosov Moscow State University, D.V. Skobeltsyn Institute of Nuclear, Physics, Moscow, Russia

[d] Department of Applied Physics, Aligarh Muslim University, Aligarh, India

[e] Institute of Theoretical Physics, University of Wroclaw, Poland